HHS Public Access

Author manuscript

Cell Stem Cell. Author manuscript; available in PMC 2022 November 02.

Published in final edited form as:

Cell Stem Cell. 2020 February 06; 26(2): 187–204.e10. doi:10.1016/j.stem.2019.11.016.

Zika Virus Targets Glioblastoma Stem Cells through a SOX2-Integrin $\alpha_v\beta_5$ Axis

Zhe Zhu[1,2,20], **Pinar Mesci**[2,3,4,20], **Jean A. Bernatchez**[5], **Ryan C. Gimple**[1,2,6,7], **Xiuxing Wang**[1,2], **Simon T. Schafer**[8], **Hiromi I. Wettersten**[2,9], **Sungjun Beck**[5], **Alex E. Clark**[10], **Qiulian Wu**[1,2], **Briana C. Prager**[1,2,6,7,11], **Leo J.Y. Kim**[1,6,7], **Rekha Dhanwani**[12], **Sonia Sharma**[12], **Alexandra Garancher**[13], **Sara M. Weis**[2,9], **Stephen C. Mack**[14], **Priscilla D. Negraes**[2,3], **Cleber A. Trujillo**[2,3], **Luiz O. Penalva**[15], **Jing Feng**[16], **Zhou Lan**[16], **Rong Zhang**[17], **Alex W. Wessel**[17], **Sanjay Dhawan**[18], **Michael S. Diamond**[17], **Clark C. Chen**[18], **Robert J. Wechsler-Reya**[13], **Fred H. Gage**[8], **Hongzhen Hu**[16], **Jair L. Siqueira-Neto**[4,*], **Alysson R. Muotri**[2,3,*], **David A. Cheresh**[9,*], **Jeremy N. Rich**[1,2,19,21,*]

[1]Department of Medicine, Division of Regenerative Medicine, University of California School of Medicine, San Diego, La Jolla, CA 92037, USA

[2]Sanford Consortium for Regenerative Medicine, 2880 Torrey Pines Scenic Drive, La Jolla, CA 92037, USA

[3]Department of Pediatrics, Rady Children's Hospital San Diego, School of Medicine, University of California, San Diego, La Jolla, CA 92307, USA

[4]Department of Cellular and Molecular Medicine, Stem Cell Program, School of Medicine, University of California, San Diego, La Jolla, CA 92307, USA

[5]Center for Discovery and Innovation in Parasitic Diseases, Skaggs School of Pharmacy and Pharmaceutical Sciences, University of California, San Diego, La Jolla, CA 92037, USA

[6]Case Western Reserve University Medical Scientist Training Program, Case Western Reserve University School of Medicine, Cleveland, OH 44106, USA

[7]Department of Pathology, Case Western Reserve University School of Medicine, Cleveland, OH 44106, USA

[*]Correspondence: jairlage@ucsd.edu (J.L.S.-N.), muotri@ucsd.edu (A.R.M.), dcheresh@ucsd.edu (D.A.C.), drjeremyrich@gmail.com (J.N.R.).

AUTHOR CONTRIBUTIONS

Z.Z., P.M., J.L.S.-N., D.A.C., A.R.M., and J.N.R. designed the experiments, analyzed the data, and wrote the manuscript with contributions from all authors. Z.Z., P.M., J.A.B., S.T.S., R.C.G., X.W., H.I.W., S.B., A.E.C., Q.W., B.C.P., L.J.Y.K., Z.L., J.F., R.Z., A.W.W., and R.D. performed the experiments. S.T.S., R.C.G., B.C.P., and L.J.Y.K. performed database analyses. S.S., S.D., C.C.C., R.J.W.-R., F.H.G., J.D.S.-N., M.S.D., and H.H. provided scientific input and helped edit the manuscript. A.G., S.M.W., S.C.M., P.D.N., C.A.T., L.O.P., R.J.W.-R., and J.L.S.-N. provided key reagents.

SUPPLEMENTAL INFORMATION

Supplemental Information can be found online at https://doi.org/10.1016/j.stem.2019.11.016.

DECLARATION OF INTERESTS

A.R.M. is a co-founder and has equity interest in TISMOO, a company dedicated to genetic analysis focusing on therapeutic applications customized for autism spectrum disorder and other neurological disorder origin genetics. The terms of this arrangement have been reviewed and approved by the University of California, San Diego in accordance with its conflict of interest policies. D.A.C. is the co-founder of TargeGen. D.A.C. is a founder of a new company, AlphaBeta Therapeutics, that is developing an antibody to integrin alphaVbeta3, involved in cancer treatment; however, this company is not yet funded. M.S.D. is a consultant for Inbios and Atreca and on the Scientific Advisory Board of Moderna.

[8]Laboratory of Genetics, Salk Institute for Biological Studies, 10010 North Torrey Pines Road, La Jolla, CA 92037, USA

[9]Department of Pathology, Moores Cancer Center, University of California, San Diego, La Jolla, CA 92037, USA

[10]Department of Cellular and Molecular Medicine and Skaggs School of Pharmacy and Pharmaceutical Sciences, University of California, San Diego, La Jolla, CA 92037, USA

[11]Cleveland Clinic Lerner College of Medicine, Cleveland Clinic, Cleveland, OH 44195, USA

[12]La Jolla Institute for Allergy and Immunology, 9420 Athena Circle, La Jolla, CA 92037, USA

[13]Tumor Initiation and Maintenance Program, NCI-Designated Cancer Center, Sanford Burnham Prebys Medical Discovery Institute, La Jolla, CA 92037, USA

[14]Department of Pediatrics, Baylor College of Medicine, Texas Children's Hospital, Houston, TX 77030, USA

[15]Children's Cancer Research Institute – UTHSCSA, San Antonio, TX 78229, USA

[16]Department of Anesthesiology, Center for the Study of Itch, Washington University School of Medicine in St. Louis, St. Louis, MO 63130, USA

[17]Departments of Medicine, Molecular Microbiology, Pathology, and Immunology and The Andrew M. and Jane M. Bursky Center for Human Immunology and Immunotherapy Programs, Washington University School of Medicine, St. Louis, MO 63130, USA

[18]Department of Neurosurgery, University of Minnesota, Minneapolis, MN 55455, USA

[19]Department of Neurosciences, University of California, San Diego, School of Medicine, La Jolla, CA 92037, USA

[20]These authors contributed equally

[21]Lead Contact

SUMMARY

Zika virus (ZIKV) causes microcephaly by killing neural precursor cells (NPCs) and other brain cells. ZIKV also displays therapeutic oncolytic activity against glioblastoma (GBM) stem cells (GSCs). Here we demonstrate that ZIKV preferentially infected and killed GSCs and stem-like cells in medulloblastoma and ependymoma in a SOX2-dependent manner. Targeting SOX2 severely attenuated ZIKV infection, in contrast to AXL. As mechanisms of SOX2-mediated ZIKV infection, we identified inverse expression of antiviral interferon response genes (ISGs) and positive correlation with integrin α_v (ITGAV). ZIKV infection was disrupted by genetic targeting of ITGAV or its binding partner ITGB5 and by an antibody specific for integrin $\alpha_v\beta_5$. ZIKV selectively eliminated GSCs from species-matched human mature cerebral organoids and GBM surgical specimens, which was reversed by integrin $\alpha_v\beta_5$ inhibition. Collectively, our studies identify integrin $\alpha_v\beta_5$ as a functional cancer stem cell marker essential for GBM maintenance and ZIKV infection, providing potential brain tumor therapy.

Graphical Abstract

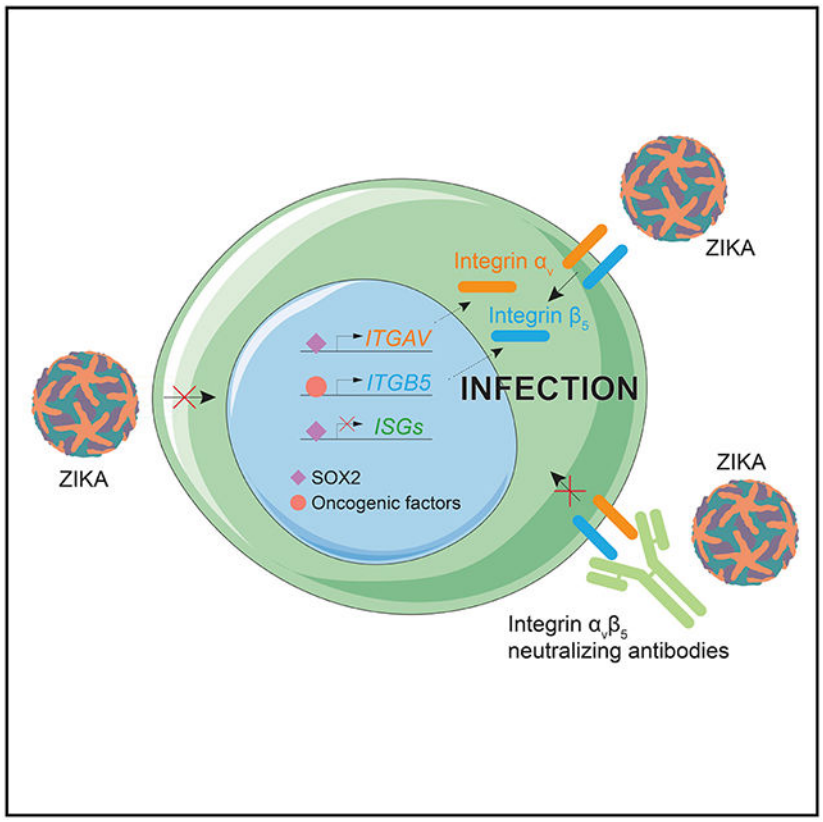

In Brief

Zika virus causes microcephaly by killing neural precursor cells but also acts as an oncolytic virus against glioblastoma. Zika preferentially targets glioblastoma stem cells through core stem cell transcription factor downregulation of innate immunity and induction of internalization through an integrin heterodimer that marks cancer stem cells.

INTRODUCTION

Glioblastoma (GBM) ranks among the most lethal of all human cancers, with current therapies offering only palliation (Stupp et al., 2005). Replication-competent oncolytic viruses have been employed against GBM and other types of brain cancer (Foreman et al., 2017). Oncolytic viruses may offer selective targeting, internalization, and killing of tumor cells while sparing normal tissues. Because GBM cells are highly invasive, preventing complete surgical resection and cure, neurotropic viruses can target cells protected from chemotherapy and other systemic therapies by the blood-brain barrier. Several oncolytic viruses have been investigated in preclinical and clinical trials for brain tumors (Russell et al., 2012). GBMs contain self-renewing, highly tumorigenic stem-like cells, called GBM stem cells (GSCs), that display preferential therapeutic resistance, invasion into normal brain tissue, stimulation of neoangiogenesis, and tumor immune escape (Singh et al., 2003; Bao et al., 2006b; Wu et al., 2010; Bach et al., 2013). Previous studies have suggested that oncolytic viruses can be engineered to target GSCs (Wakimoto et al., 2009; Allen et al.,

2013; Bach et al., 2013; Zemp et al., 2013; Josupeit et al., 2016). Thus, we hypothesized that an oncolytic virus targeting effort could be optimized by leveraging neurotropic viruses that preferentially target specific cell types, such as neural precursor cells (NPCs).

In 2015, a Zika virus (ZIKV) epidemic in Central and South America became a global health emergency (Heymann et al., 2016) following a dramatic increase in the number of newborns with microcephaly and other congenital anomalies (Nowakowski et al., 2016; Oliveira Melo et al., 2016; Schuler-Faccini et al., 2016). Infected adults are often asymptomatic, whereas ZIKV infection of pregnant mothers can be associated with developmental and neurological disorders in subsequent live births (Petersen et al., 2016). The neurotropism and neurovirulence of ZIKV have been appreciated in model systems, confirming a causal link between ZIKV and birth defects (Lazear et al., 2016; Li et al., 2016; Miner et al., 2016). Numerous studies have shown that different cell populations in the nervous and immune systems are differentially susceptible to ZIKV infection (Retallack et al., 2016; Tang et al., 2016; Foo et al., 2017; Michlmayr et al., 2017; Oh et al., 2017; Zhu et al., 2017; Chen et al., 2018a; Mesci et al., 2018). One challenge in predicting the tropism of ZIKV has been the lack of a consistent molecular pathway mediating cellular infection of ZIKV. AXL has been proposed to mediate ZIKV infection of astrocytes but not NPCs via bridging by its natural ligand, Gas6 (Meertens et al., 2017), but AXL may have only indirect effects on ZIKV infection of astrocytes because of its role in modulating antiviral immunity (Chen et al., 2018a). To date, the identity of the ZIKV entry factor remains controversial (Nowakowski et al., 2016; Wells et al., 2016; Chen et al., 2018a).

We recently reported that ZIKV selectively kills patient-derived GSCs compared with differentiated GBM cells (DGCs) in culture, tumor organoids, and slice cultures (Zhu et al., 2017). These observations have been confirmed by others (Kaid et al., 2018; Chen et al., 2018b). Although the use of wild-type ZIKV is unlikely to be directly translated into clinical use for GBM patients, we hypothesized that interrogating the molecular mechanisms of ZIKV in GSCs could not only improve the potential application of future modified ZIKV in neuro-oncology but also elucidate mechanisms by which ZIKV gains entry into brain cells.

RESULTS

ZIKV Preferentially Infects and Kills Brain Tumor Stem Cells

To determine the potential of ZIKV to achieve preferential anti-tumor efficacy against GSCs with limited toxicity for normal brain, we compared ZIKV infection of GSCs with human NPCs derived from either induced pluripotent stem cells (iPSCs) or primary tissues. ZIKV preferentially infected patient-derived GSCs, as quantified by both detection of ZIKV envelope protein (ZIKV-E) (Figures 1A–1C) and viral RNA (Figures 1D and 1E). Although the infection of GSCs was moderately higher than that of normal NPCs, ZIKV induced greater cell death in GSCs (Figures 1F–1I). ZIKV reduced GSC numbers through induction of apoptotic cell death and reduced proliferation (Figures 1J–1L, S1M, and S1N). These results were validated in a panel of 5 GSCs and 5 NPCs from different genetic backgrounds (Figures S1A–S1I and S1N). Although NPCs were less sensitive to ZIKV than GSCs, NPCs were killed by ZIKV, but over a longer time course than GSCs (Figures S1J–S1L and

S1N), associated with mildly lower apoptosis (Figure S1O) and induction of differentiation (Figures S1O and S1P).

GBMs represent the brain cancer for which the tumor hierarchy is most clearly delineated, but other brain tumors, especially pediatric brain tumors, contain stem-like tumor cells (Bao et al., 2006a; Mack et al., 2018). We interrogated the anti-tumor efficacy of ZIKV against 2 pediatric pontine gliomas, 4 medulloblastomas, an ependymoma, and 2 meningiomas grown under serum-free conditions to enrich for stem-like populations (Wang et al., 2017a). For all models except meningiomas, ZIKV induced apoptotic cell death (Figures 1M and S2A–S2C). Unlike the other tumor types tested, meningioma is not intrinsic to the brain parenchyma; it is posited to arise from the arachnoid granulations (Buetow et al., 1991). Collectively, these results establish preferential ZIKV killing of stem-like brain tumor cells, supporting its potential utility as a platform for an oncolytic virus.

SOX2 Modulates Infection of GSCs Associated with Repression of Innate Antiviral Responses

To define the molecular determinants of ZIKV infection of GSCs, we investigated a core regulator of GSCs reported to mark NPCs infected by ZIKV, SOX2 (Souza et al., 2016). SOX2 is an SRY-box transcription factor that is expressed at high levels during neural development and contributes to induced pluripotency (Sarkar and Hochedlinger, 2013). GSCs express high levels of SOX2, and targeting SOX2 expression attenuates GSC maintenance (Gangemi et al., 2009). Nearly all ZIKV-infected NPCs and GSCs were $SOX2^+$, and most $SOX2^+$ cells were infected by ZIKV (Figures 2A and 2B). The fraction of ZIKV-infected cells mirrored the fraction of $SOX2^+$ cells in other brain tumor types (Figures S2D and S2E); meningioma cultures had both the lowest fraction of $SOX2^+$ cells and ZIKV infection. GSCs expressed higher levels of SOX2 than NPCs by immunoblot (Figure S2F).

To address the functional role of SOX2 in ZIKV infection, we targeted SOX2 expression using two non-overlapping short hairpin RNAs (designated shSOX2.52 and shSOX2.53) relative to a control short hairpin RNA (shRNA) sequence designed to avoid targeting any sequence in the mammalian genome (shCONT) (Figure S2G). Consistent with its role in GSC maintenance, targeting SOX2 expression induced expression of the differentiation marker GFAP (Figure S2G). GSCs transduced with shCONT retained their ability to be infected by ZIKV, as measured by both ZIKV-E protein and RNA, whereas GSCs transduced with shSOX2 showed attenuated ZIKV infectivity (Figures 2C–E). Although AXL is a putative ZIKV receptor (Nowakowski et al., 2016), we did not observe differential ZIKV infection following AXL knockdown, suggesting that AXL is dispensable for ZIKV infection of GSCs (Figures 2C, 2D, and S2H). Moreover, in GBM surgical specimens, the majority of AXL^+ cells were $GFAP^+$, not $SOX2^+$, suggesting that SOX2 and AXL mark discrete tumor populations (Figures S2I and S2J).

SOX2 exerts many of its effects through transcriptional regulation of gene targets. To focus our efforts on mediators of ZIKV infection, we interrogated The Cancer Genome Atlas (TCGA) GBM database for genes that correlated with *SOX2* mRNA expression. *SOX2* positively correlated with genes involved in nervous system development and neuronal structural components, whereas *SOX2* negatively correlated with genes of the innate

immune response and regulation (Figures 2F and 2G). Because suppression of cell-intrinsic innate immune responses can render cells susceptible to viral infection, we interrogated the relationship between SOX2 mRNA expression and mediators of the interferon-stimulated gene (ISG) family. *SOX2* mRNA consistently negatively correlated with ISGs in GBM (Figures 2H, 2I, and S3A). Silencing SOX2 induced ISG expression, supporting SOX2 regulation of antiviral cellular responses (Figures 2J and S3B). To determine whether these changes in ISGs were biologically relevant, we examined ISG levels in GSCs treated with increasing concentrations of type I interferon (Figure S3C). The inverse relationship between SOX2 and ISGs in GSCs contrasts with normal stem cells, where ISGs are highly expressed (Wu et al., 2018), suggesting that SOX2 function differs between normal and neoplastic stem cells.

SOX2 Regulates Integrin α_v Expression in GSCs

SOX2 suppression of the innate antiviral response provides one mechanism by which its expression correlates with ZIKV infection. We hypothesized that SOX2 also may regulate the expression of molecules involved in the primary infection process, based on the rapid decrease in ZIKV infection after SOX2 targeting, so we interrogated the TCGA GBM database for associations between *SOX2* mRNA, expression of other GSC markers, and possible ZIKV receptors, including the TAM receptors (*TYRO3*, *AXL*, and *MERTK*) and several integrins, which may serve as attachment factors for West Nile virus and other flaviviruses (Chu and Ng, 2004; Meertens et al., 2017; Figure 3A). *AXL* and *SOX2* expression were not correlated, whereas the mRNA levels of integrin α_v (*ITGAV*) correlated with *SOX2* and other GSC markers (*NES*, *PAX6*, and *OLIG2*) (Figures 3A and S4A). Because SOX2 is a transcription factor, we investigated SOX2 regulation of ITGAV. Measurement of active chromatin through histone 3 lysine 27 acetyl chromatin immunoprecipitation followed by deep sequencing (H3K27ac ChIP-seq) of GSCs and DGCs revealed activation of the ITGAV locus in GSCs, whereas the AXL locus was more activated in DGCs (Suvà et al., 2014; Figure 3B); these data were consistent with the immunofluorescence staining of GBMs (Figure S2I). SOX2 bound within the *ITGAV* locus by ChIP-seq, and its binding was associated with an increase in the active chromatin mark H3K27ac at this locus (Figure 3B). ChIP-PCR of SOX2 on the *ITGAV* locus in a set of GSCs confirmed SOX2 binding (Figure 3C). Gene silencing of SOX2 using either of two non-overlapping shRNAs showed reduced ITGAV expression but not that of another integrin subunit, *ITGB5*, as measured by mRNA levels, immunohistochemistry, and immunoblotting (Figures 3D, S4B, and S4C). Collectively, these results demonstrate that SOX2 regulates ITGAV expression in GSCs.

Blockade of $\alpha_v\beta_5$ Integrin Reduces ZIKV Infection in GSCs

The integrin α_v subunit forms heterodimers with one of five different β subunits (β_1, β_3, β_5, β_6, or β_8) to mediate its binding to matrix ligands and promote intracellular signaling, adhesion, cell migration, and cell proliferation (Desgrosellier and Cheresh, 2010). To determine whether any of the integrin heterodimers were involved in ZIKV infection, we screened a panel of function-blocking antibodies against different integrins—pan-β_1 (P4C10), $\alpha_v\beta_3$ (LM609), and $\alpha_v\beta_5$ (P1F6)—for the capacity to prevent viral infection. Although blocking antibodies against β_1 and $\alpha_v\beta_3$ integrins had limited effect on ZIKV

infection of NPCs or GSCs, as measured by ZIKV-E staining (Figures 3E and S4D) or ZIKV RNA levels (Figure 3F), blockade of $\alpha_v\beta_5$ integrin substantially reduced viral infection (Figures 3E, 3F, and S4D–S4G). Although blocking antibodies against β_1 and $\alpha_v\beta_3$ integrins did not alter surface binding or internalization of ZIKV to GSCs, a blocking antibody against integrin $\alpha_v\beta_5$ reduced ZIKV internalization to a greater extent than cell binding (Figure 3G). We assessed the effects of antibody blocking of integrins on ZIKV killing of NPCs and GSCs. With blocking antibodies against β_1 or $\alpha_v\beta_3$ integrins, we observed similarly reduced cellular viability with increasing multiplicity of infection (MOI) compared with a control antibody (Figure 3H). In contrast, a blocking antibody against $\alpha_v\beta_5$ integrin attenuated ZIKV-mediated cell death in both NPCs and GSCs (Figures 3H, S4H, and S4I). The $\alpha_v\beta_5$ integrin-blocking antibody also attenuated ZIKV effects on sphere formation under serum-free conditions (Figure 3I).

Brain organoids are complex, three-dimensional structures that self-organize and provide models that share features with normal and neoplastic brain tissues (Drost and Clevers, 2018); they have proven useful for studying viral infections (Zhou et al., 2018), including ZIKV (Garcez et al., 2016; Qian et al., 2016). We recently reported GBM organoids as a system for investigating the basis of GBM heterogeneity (Hubert et al., 2016). GBM organoids grow over time, as measured by organoid diameter (Figures S4K and S4L). Supporting a functional importance for $\alpha_v\beta_5$ integrin in GBM growth, tumor organoids incubated with an integrin $\alpha_v\beta_5$-blocking antibody were static or reduced in size over time. In contrast, tumor organoids infected with ZIKV were obliterated, an effect that was lost upon treatment with the $\alpha_v\beta_5$ integrin-blocking antibody (Figures S4K and S4L).

To determine whether GBMs preferentially express specific integrins, we interrogated the TCGA GBM dataset, which revealed that α_v and β_1, β_3, β_5, and β_8, but not β_6 integrin subunits, were overexpressed in GBM relative to normal brain (Figure 4A). The preferential expression of these integrins suggested that they might contribute to the specificity of ZIKV infection, so we silenced expression of the β subunits known to associate with integrin α_v (β1, β_3, β_5, β_6, or β_8) using two non-overlapping shRNAs each (Figure 4B). Only silencing of integrin β_5 prevented killing of GSCs by ZIKV infection, as measured by cell viability (Figure 4C), sphere formation (Figure 4D), sphere size (Figure 4E), and ZIKV RNA copy number (Figure 4F). In complementary studies, we targeted ITGB3, ITGB5, and ITGAV using CRISPR/Cas9 gene editing (Figure S5A), revealing that ZIKV infection required ITGAV and ITGB5 but not ITGB3 (Figure S5B). We previously demonstrated that integrin α_6 (ITGA6) is a functional GSC marker (Lathia et al., 2010). Targeting ITGAV by CRISPR/Cas9 did not change ITGA6 levels (Figures S5C and S5D). Targeting ITGA6 by CRISPR/Cas9 reduced ITGA6 expression and the number of GSCs, consistent with our previous study (Figures S5E–S5G). Although ITGA6 single-guide RNA (sgRNA) and ZIKV infection both targeted GSCs (Figure S5G), GSCs surviving loss of ITGA6 were not infected by ZIKV at higher rates, and ZIKV infection did not specifically deplete $ITGA6^+$ cells in surviving GSCs (Figures S5H and S5I), suggesting that ITGA6 is not essential for ZIKV infection of GSCs. Collectively, these results support a specific role for $\alpha_v\beta_5$ integrin in ZIKV infection and cellular killing.

$\alpha_v\beta_5$ Integrin Maintains GSCs

To interrogate the role of integrin $\alpha_v\beta_5$ in GSCs, we leveraged a panel of H3K27ac profiles that we developed from primary GBM resection specimens (Wang et al., 2017b) and compared these with normal brain H3K27ac profiles derived from the Roadmap Epigenomics database (Figure 5A). The loci for *SOX2*, *ITGAV*, and *ITGB5* displayed more active chromatin states in GBM than non-neoplastic brain. AXL, in contrast, showed similar chromatin states between tumor and non-neoplastic tissues (Figure 5A). High *ITGB5* mRNA levels were associated with a poor prognosis in IDH1 wild-type GBM patients, with a particularly poor prognosis for patients with high levels of both *ITGAV* and *ITGB5* (Figure 5B). To further link SOX2 and $\alpha_v\beta_5$ integrin in GBM, we performed immunofluorescence for SOX2, $\alpha_v\beta_5$ integrin, and GFAP (a marker of differentiated cells) on surgical specimens from GBM and control brain tissue derived from epilepsy patients (Figure 5C). GBM tissues had more integrin $a_vb_5^+$ cells than non-neoplastic brain, and the majority of $SOX2^+$, but not $GFAP^+$, cells expressed $\alpha_v\beta_5$ integrin (Figure 5D). CRISPR/Cas9 targeting of ITGAV with two distinct sgRNAs (sgITGAV) in GSCs reduced integrin $\alpha_v\beta_5$ protein expression, as measured by immunofluorescence, but not SOX2 expression, supporting that ITGAV is downstream of SOX2 (Figure 5E). As expected, GSCs transduced with sgITGAV had reduced surface expression of $\alpha_v\beta_5$ integrin (Figure 5F). Targeting ITGAV attenuated GSC viability (Figure 5G) and self-renewal, as measured by limiting dilution sphere formation (Figures 5H and 5I). Immunocompromised mice bearing two different GSCs transduced with one of two sgITGAVs survived longer and had reduced tumor growth compared to a control sgRNA (sgCONT) (Figures 5J and 5K). These results demonstrate that the cells targeted by ZIKV and marked by ITGAV expression are critical to tumor growth.

ZIKV Induces Cellular Changes in Normal Mature Cerebral Organoids but Has Little Effect on Size

To avoid species differences between tumor and normal cells, we determined the relative effects of ZIKV infection on GBM and normal cerebral organoids. Mature brain cortical organoids (BCOs) from human pluripotent stem cells (Thomas et al., 2017; Trujillo et al., 2019) contain mature neurons from different layers (CTIP2, NeuN, SATB2, and $MAP2^+$ cells) and neuronal progenitors ($SOX2^+$) and glia ($GFAP^+$) (Figures 6A and S6A). ZIKV had little effect on the size of BCOs over time (Figures 6B, 6C, and S6B), but there was an increase in apoptotic cells and decrease in $SOX2^+$ cells (Figures 6D and 6E). ZIKV had little to no effect on the proportions of different neuronal and astrocytic cell types in cerebral organoids (Figures 6F–6I).

Generation of Human GBM-Cerebral Organoid Models

To test the relative efficacy of ZIKV infection against human GBM relative to toxicity to normal human brain, we implanted human GBM tumors grown in mature (6-month-old) human BCOs. After 6 months, most NPCs differentiated into neurons and astrocytes (Thomas et al., 2017; Trujillo et al., 2019). Mimicking tumor growth, the GFP-GSCs invaded the BCOs and expanded over time (Figure 6J). The cerebral organoids alone without GSCs displayed substantially lower expression of $\alpha_v\beta_5$ integrin than the GBM organoids (Figures 6K and 6L). The GFP-GSCs preferentially expressed SOX2 and $\alpha_v\beta_5$ integrin

relative to normal BCO cells (Figures 6M and 6N). These results demonstrate that fused GSC-BCOs preserve the differential expression profiles found in human tumors and normal brain and offer a platform to study human GBM.

ZIKV Infection Preferentially Targets GSCs in GBM-BCOs

ZIKV infection of GBM-BCOs preferentially reduced GFP-GSCs (Figure 6O) and infected $\alpha_v\beta_5$ integrin$^+$ cells in combined GBM-BCOs, reducing the number of GFP-labeled tumor cells (Figures 6P and 6Q). In 2 patient-derived GSCs fused with human BCOs, ZIKV showed a potent anti-tumor effect over time (Figures S7A and S7B). We followed the number of GFP-GSCs by measuring the integrated density of GFP$^+$ cells (Figures S7A and S7B) and immunostaining of GFP$^+$ cells (Figures 6R and S7C); this showed preferential infection of GSCs by ZIKV and reduced cell numbers. Upon ZIKV infection, GFP-GSC-BCOs had an increased number of ZIKV-E$^+$ cells that were mainly seen in GFP$^+$ cells (Figures 6R and S7C). To rule out a contribution of GFP to the increased vulnerability of GFP-labeled GSCs to ZIKV infection, we generated GFP-BCOs by transducing iPSCs with a phosphoglycerate kinase (PGK) promoter-driven GFP lentivirus and then infected them with ZIKV (Figure S7D). ZIKV decreased the fraction of GFP$^+$ cells in GFP-GSC-BCOs, concomitant with GSC apoptosis (Figure S7E), but not the number of GFP$^+$ cells in GFP-BCOs (Figure S7F), confirming that GSC vulnerability to ZIKV in GSC-BCOs is not due to the presence of GFP. Given the regulation of ISGs by SOX2 in cell culture, we interrogated our GBM-BCOs for immune responses after infection with ZIKV by performing targeted RNA sequencing using a Nanostring panel of 770 immune-related genes (Figure 6S). Upon infection with ZIKV, 113 genes were differentially expressed, including increased expression of several ISGs as well as inflammasome, adaptive immunity, antigen presentation, interferon (IFN) response, and Toll-like receptor (TLR) signaling pathways (Figure 6T and 6U), suggesting that organoids induce an immune response associated with elimination of GSCs by the virus. Collectively, these results confirm that ZIKV has oncolytic activity against GSCs and that this is associated with preferential expression of $\alpha_v\beta_5$ integrin in a fully humanized model system.

ZIKV Does Not Induce Malignant Transformation in Normal Brain but Targets GSCs *In Vivo*

To address the potential for ZIKV induction of malignancy *in vivo*, we tested its toxicity on NPCs and the potential for oncogenic transformation of normal NPCs using 4- to 6-week-old immunocompromised mice (non-obese diabetic [NOD].Cg-*Prkdc*^{scid}*Il2rg*^{tm1Wjl}/SzJl [NSG]). ZIKV (10^3 focus-forming units [FFU]/mouse of either the Human Panama [HPAN] or Puerto Rican isolate of ZIKV [PRVABC-59] [PRV] strains) was inoculated directly into the subventricular zone (SVZ). 72 h later, ZIKV infection of murine NPCs in the SVZ was confirmed through co-localization of ZIKV-E with the NPC marker SOX2 and $\alpha_v\beta_5$ integrin staining (Figures 7A and 7B). One month after ZIKV inoculation, the immunocompromised mice reached endpoint criteria (neurological signs), likely because of ZIKV virulence (Figure 7C). Analysis of ZIKV-infected brains revealed no gross morphological changes or evidence of malignancy (Figure 7D). These findings suggest that ZIKV induces neural toxicity *in vivo* in NSG mice but does not cause oncogenic transformation.

Previous reports from our laboratory and others have shown that ZIKV kills GSCs *in vivo* (Zhu et al., 2017; Kaid et al., 2018; Chen et al., 2018b). To assess the role of $\alpha_v\beta_5$ integrin in ZIKV-dependent oncolytic activity against GSCs *in vivo*, we used a tumor transplantation model in NSG mice and two complementary techniques: pharmacological inhibition with an integrin $\alpha_v\beta_5$-blocking antibody and genetic targeting of integrin β_5 expression using CRISPR/Cas9-based techniques. GSCs treated with an immunoglobulin G (IgG) control antibody had the shortest survival, whereas treatment with ZIKV extended the survival of tumor-bearing hosts (Figures 7E and 7F). Treatment of GSCs with an antibody targeting $\alpha_v\beta_5$ or gene editing of ITGB5 in the tumor attenuated Zika-mediated cytotoxicity and reduced host survival (Figures 7E and 7F). However, treatment with the $\alpha_v\beta_5$ integrin-blocking antibody extended the survival of tumor-bearing hosts in the absence of ZIKV treatment, which is consistent with the independent role of $\alpha_v\beta_5$ integrin in GSC maintenance. Collectively, these results support a role of integrin $\alpha_v\beta_5$ in ZIKV-dependent targeting of GSCs *in vivo*.

Blocking $\alpha_v\beta_5$ Integrin Inhibits ZIKV Infection in Patient-Derived Tissues

Finally, to rule out possible effects of culture of tumors, we infected fresh intraoperative patient-derived GBM slices with ZIKV. To establish this model, we obtained freshly isolated primary human GBM slices and then incubated them with either an IgG control antibody or blocking integrin antibodies and infected them with ZIKV. Attenuation of ZIKV infection by $\alpha_v\beta_5$ integrin blockade was confirmed by staining for the ZIKV-E protein (Figure 7G) and quantifying the levels of ZIKV RNA (Figure 7H). These data support a dependence of $\alpha_v\beta_5$ integrin on ZIKV infection of GBM.

DISCUSSION

Identification of molecular mediators of viral infection is important for antiviral and oncolytic virus strategies (Medigeshi et al., 2008; Brinton, 2013). Enrichment strategies for effective oncolytic therapy trials now include testing for expression of key determinants of viral infection in tumor tissues prior to patient enrollment. Here we demonstrate that SOX2 and integrin $\alpha_v\beta_5$ mark GSCs that are preferentially targeted by ZIKV in association with suppression of immune response genes and a molecular complex involved in viral internalization. α_v integrins are a particularly attractive set of targets for several reasons. These integrins are often expressed at low levels in normal tissues, with induction upon stress environments found in tumors (Desgrosellier and Cheresh, 2010). Further, integrins can be modulated with acceptable toxicity through neutralizing antibodies or small molecules. More than two decades ago, these integrins were linked to adenovirus infection (Wickham et al., 1993). More recently, selected integrins have been associated with viral infection of other viruses in the flavivirus family, albeit with differential results based on assay (Schmidt et al., 2013; Fan et al., 2017). α_v integrins have been linked to cancer stem cells; integrin $\alpha_v\beta_3$ is expressed in epithelial cancer stem cells, where it serves as a driver of tumor initiation and drug resistance (Seguin et al., 2014, 2017). In GBM, $\alpha_v\beta_3$ expression inhibits senescence (Poirot et al., 2015) and facilitates glucose uptake by promoting upregulation of the high-affinity glucose transporter Glut3 (Cosset et al., 2017). ZIKV infection was not inhibited by shRNAs or sgRNAs against ITGB3 or LM609, a highly

selective antibody antagonist of $\alpha_v\beta_3$. Instead, our results suggest that a specific integrin heterodimer, $\alpha_v\beta_5$, closely related to $\alpha_v\beta_3$, is required for optimal ZIKV infection in GSCs. Although α_v integrin also is expressed by NPCs, expression of the β_5 integrin subunit is more selective to GBM, both stem-like and differentiated tumor cells. Therefore, GSCs display preferential sensitivity to ZIKV based on one integrin that is linked to a stem-like state and its partner, which is linked to a neoplastic state.

Our studies suggest an additional molecular mechanism mediating the effects of ZIKV against GSCs: downregulation of the antiviral immune response by SOX2, a core regulator of GSCs. These results stand in contrast to high expression levels of several ISGs in embryonic stem cells and more restricted ISG expression in neural stem cells, which have high levels of SOX2 expression (Wu et al., 2018). The divergent results between GSCs and normal stem cells suggest that SOX2 transcriptional control of ISGs is likely defined by other levels of control, including co-binding of other transcription factors and differential chromatin states. Comparison of the chromatin landscapes of GSCs and NPCs revealed that GSCs have greater activation of chromatin across the genome, which can alter transcriptional regulation (Mack et al., 2019). To further consider the role of immune responses in GSCs upon ZIKV infection, we interrogated transcriptional regulation of immunological modulators of GSCs grown in organoids with normal brains, which demonstrated upregulation of genes in the inflammasome, adaptive immune responses, TLR signaling, and IFN responses. Although SOX2 does not solely determine GSC response to ZIKV, GSCs appear to be less immunogenic than DGCs, offering a potential advantage in sustained tumor growth in the inflammatory environment found in GBMs. This immune phenotype may offer a potential selection factor.

Here we extend the recent description of GBM-BCO systems by another group (Ogawa et al., 2018). We leveraged the system to model the growth patterns of patient-derived models and test the efficacy of antitumor therapies. This system is particularly valuable for measuring the direct therapeutic index of therapies, such as oncolytic viruses, that must provide substantial anti-tumor activity while minimizing toxicity against normal tissues, like the brain. Because some viral infections display strong species specificity, the use of human GBMs in organoids of normal human brain may empower greater relevance of selective tumor targeting in preclinical studies. Further, we employed genetic and pharmacologic targeting strategies that can be leveraged to dissect the determinants of tumor response to oncolytic viral therapies.

Although direct application of wild-type ZIKV as an oncolytic virus in GBM would likely be challenging, we and others have already reported that genetically attenuating modifications to ZIKV strains may offer reduced toxicity against normal tissues (Zhu et al., 2017; Chen et al., 2018b). Identification of SOX2-associated downregulation of the innate antiviral immune response that distinguishes normal and neoplastic stem cells and of integrin $\alpha_v\beta_5$ as an important molecular feature mediating infection may prioritize selection of genetically modified ZIKV for use in patients to augment efficacy against the most resistant and aggressive GBMs cells while minimizing virus-induced disease.

STAR★METHODS

LEAD CONTACT AND MATERIALS AVAILABILITY

All data will be provided to reviewers and/or editors upon request. There are no restrictions on data availability. Further information and requests should be addressed to and will be fulfilled by the Lead Contact, Jeremy Rich (drjeremyrich@gmail.com).

EXPERIMENTAL MODEL AND SUBJECT DETAILS

Ethical Compliance Statement—For intracranial tumor models, NSG (NOD.Cg-*Prkdc*^{scid}*Il2rg*^{tm1Wjl}/SzJl, #005557, Jackson Laboratory, Bar Harbor, ME) mice were used under the University of California, San Diego Institutional Animal Care and Use Committee (IACUC) approved protocol. All experiments conformed to the ethical and humane standards for animal treatment as defined by our protocol. Animals were monitored daily and were humanely sacrificed upon the appearance of any neurological signs.

Culture of GSCs, DGCs, and nonmalignant brain cultures—Glioblastoma tissues were obtained from excess surgical materials from patients at the Cleveland Clinic after neuropathology review with appropriate consent, in accordance with an IRB-approved protocol. To prevent culture-induced drift, patient-derived xenografts were generated and maintained as a recurrent source of tumor cells for study (Wang et al., 2017a). To prevent culture-induced drift in GBM models, patient-derived subcutaneous xenografts were generated in NOD.Cg-*Prkdc*^{scid}*Il2rg*^{tm1Wjl}/SzJl mice (#005557, Jackson Laboratory) and maintained as a recurrent source of tumor cells for study. Upon xenograft removal, a papain dissociation system (Worthington Biochemical) was used to dissociate tumors according to the manufacturer's instructions. Cells were then cultured in Neurobasal complete media (Neurobasal medium; Life Technologies) supplemented with 1 × B27 without vitamin A (Thermofisher), 2 mM l-glutamine (Thermofisher), 1 mM sodium pyruvate (Thermofisher), 20 ng/ml basic fibroblast growth factor (bFGF), and 20 ng/ml epidermal growth factor (EGF; R&D Systems). The GSCs phenotype was validated by OLIG2 and SOX2 expression, functional assays of self-renewal (serial neurosphere passage), and tumor propagation using *in vivo* limiting dilution. All cells were incubated at 37°C in humidified incubators supplemented with 5% CO_2 and tested to ensure that they were negative for mycoplasma. See also Table S1 for GSCs lines.

Proliferation and neurosphere formation assay—Cell viability was measured using CellTiter-Glo (Promega) according to the manufacturer's instructions. All data were normalized to day 0, prior to infection with ZIKV, and expressed as a relative cell number. Neurosphere formation was measured as previously described (Wang et al., 2017b, 2018). Briefly, decreasing numbers of cells per well (50, 20, 10, 5, and 1) were plated into 96-well plates. Seven days after plating, the presence and number of neurospheres in each well were recorded. Extreme limiting dilution (ELDA) analysis was performed using software available at http://bioinf.wehi.edu.au/software/elda (Wang et al., 2017a, 2018).

Brightfield images—GFP-GSC, GSCs and BCOs images were acquired on an EVOS cell imaging microscope (Thermofisher). Images were acquired using an ImageXpress Micro

automated microscope (Molecular Devices) and exported using MetaXpress 5.3 (Molecular Devices).

Immunohistochemistry, immunofluorescence, and microscopy—Ten μm-thick cryosections were air-dried and fixed in 3.7% paraformaldehyde (PFA) for 15 minutes before being washed twice with PBS. Tissues were permeabilized by incubating the slides with 1% Triton X-100 in PBS for 15 minutes at room temperature. After blocking for 1 hour at room temperature in a blocking buffer containing 0.25% Triton X-100, 2.5% BSA in 1 × PBS, slides were incubated overnight in a humidified chamber at 4°C with primary antibodies for ZIKV (Millipore; AB10216; working dilution 1:1,000), SOX2 (Millipore; AB5603; stock: 1 mg/ml; working dilution 1:400), GFAP (Invitrogen, PA5–18598; working dilution 1:1,000), AXL (Abcam; AB32828; stock: 1 mg/ ml; working dilution 1:200), TUBB3 (Thermofisher; MA1–118; working dilution 1:500) and MAP2 (Abcam; ab5392, working dilution 1:2000). After 1xPBS washes, slides were incubated with Alexa Fluor 488–, 594–, or 647–conjugated anti–mouse, anti–rat, anti-goat, or anti–rabbit secondary antibodies (Thermofisher, working dilution 1:1000). Slides were subsequently washed and mounted using VECTASHIELD with DAPI (Vector Laboratories). For immunocytochemistry stainings, 10^5 cells were seeded into a 12-well chamber slide (Thermofisher) and cultured overnight. Slides were then processed as described previously for tissue staining. 10 ×, 20 ×, and 40 × images were collected at room temperature on Zeiss Apotome microscope. The cells were identified based on DAPI. Image analysis was performed by thresholding for positive staining and normalizing to total tissue area using ImageJ and Zen (Zeiss) software. Quantification was performed in a blinded manner to eliminate bias.

EdU labeling and imaging—The EdU labeling was performed according to the manufacturer's instructions (Thermofisher). Briefly, cells were plated on coverslips and allowed to recover overnight. A final concentration of 10 μM EdU was added (Click-iT EdU imaging Kit, molecular probes). The cells were then incubated for 1 hour at 37°C. After incubation, the media was removed and 0.5 mL of 3.7% paraformaldehyde was added in PBS to each well containing the coverslips. The cells were then incubated for 15 minutes at room temperature. The paraformaldehyde was removed, and the cells were washed twice with 1 mL of 3% BSA in PBS. The wash solution was then removed and 1 mL of 0.5% Triton® X-100 in PBS (permeabilization buffer) was added to each well, then incubated at room temperature for 20 minutes. The permeabilization buffer was then removed, the cells were washed twice with 1 mL of 3% BSA in PBS. Finally, 0.5 mL of Click-iT® reaction cocktail was added to each well containing a coverslip. The plate was briefly rocked to ensure that the reaction cocktail was distributed evenly over the coverslip for 30 minutes at room temperature, protected from light. After 30 minutes, the reaction cocktail was removed, cells were washed once with 1 mL of 3% BSA in PBS before proceeding to DNA staining (DAPI, Vector Laboratories H-1200) and imaging (Zeiss Apotome).

ZIKV preparation—ZIKV human isolates H/PAN/2016/BEI-259634 and PRVABC59 (BEI Resources, NR-50210 and NR-50240) from Panama and Puerto Rico, respectively, were acquired from the ATCC and distributed by BEI. Viruses were amplified in Vero

cells, totaling 2–3 serial passages of the original viral stock. Infected cell supernatants were concentrated through a 30% sucrose cushion, and re-suspended in neural maintenance medium base (50% DMEM/F12 Glutamax, 50% Neurobasal medium, 1x N2 Supplement, 1x B27 Supplement all from Life Technologies) supplemented with 1% DMSO and 5% FBS and stored at −80°C. Viral stock titers were determined by plaque assay on Vero cells and were greater or equal to 2×10^8 plaque forming units/ml. Mock media was prepared by concentrating uninfected Vero cell supernatant as above.

ZIKV titration—Viral titers (plaque forming units (FFU)/mL) were calculated by plaque-forming assays on Vero cells. Vero cells were seeded at a density of 7.5×10^4 cells per well in standard 24-well plates and incubated at 5% CO_2, 37°C for 48 hours before infection. Serial dilutions of supernatants were collected from ZIKV-infected NPCs and GSCs after infection with ZIKV at MOI of 0.1 FFU/cell, and then added to Vero cells for 1 hour. Cells were covered with an agarose overlay and further incubated for 72 hours. 3.7% paraformaldehyde was added on top of overlays for 24 hours to fix monolayers, overlays were removed, and cell monolayers were stained with crystal violet to visualize plaques.

***In vitro* viral infection—**GSCs were plated at 5,000 cells/well in 96-well tissue culture plates and allowed to attach overnight. For viral infection and growth inhibition assays, ZIKA.HPAN and ZIKA.PRV at a range of MOI 0.1, 1, and 5 FFU/cell.

Zika viral RNA quantification—Quantitative real-time PCR (qRT-PCR) was performed using primers, probes, RNA standards, and conditions described previously (Boonnak et al., 2008). Briefly, Viral RNA was extracted from cell culture using the QIAamp Viral RNA Mini Kit (QIAGEN, Valencia, CA). ZIKV RNAs were detected using TaqMan® Universal Master Mix II, no UNG (Thermofisher). The samples were carried out in 20 μL reactions and the run method was as follows: 10 minutes at 95°C, 42 cycles of 15 s at 95°C followed by 1 minute at 58°C. The sensitivity of the ZIKV real-time assays was evaluated by titration of serial dilution of virus with a previously known titer. GraphPad Prism was used as fitting software. See also Table S2 for the ZIKV primers.

Binding and internalization assay—To measure ZIKV cell surface binding/adsorption, the GSCs and hNPCs incubated with indicated integrin receptor neutralizing antibodies at 50 mg/ml for 1 hour at 4°C, were exposed to ZIKV at a MOI of 5 FFU/cell, along with serum-only and media-only controls for 1 hour at 4°C. Cells were washed three times at 4°C with 10 mL PBS containing 10% BSA. The number of viruses that bound to the cells was determined by qRT-PCR. To measure ZIKV immune complex internalization, cells were exposed to ZIKV at MOI of 5 FFU/cell. The cells were washed three times with 10 mL PBS and resuspended with PBS containing 10% BSA. The cells were treated with 5 mg/ml of Pronase (Roche Applied Science, Indianapolis, IN) to remove excess virus on the cell surface. The number of internalized viruses was determined by qRT-PCR (Boonnak et al., 2008).

Lentiviral shRNA transfection—shRNA sequences were selected from the Mission 2.0 library (Sigma-Aldrich). Plasmids were transformed and amplified in Dh5α competent *E. coli* and purified using EndoFree Plasmid mini kit (Omega, #D6948). For lentivirus

preparation, 293T cells were seeded in 6-well plates and transfected with shRNA against SOX2, AXL vectors and Mission Lentiviral Packaging Mix (Sigma-Aldrich, #SHP001) using JetPrime transfection reagent (Polyplus, #89129–926). After 24 hours, growth media was changed to Neurobasal media and after 48 hours, supernatants were collected and GSCs were infected. After 48 hours of infection, GSCs were trypsinized and reseeded on a 96-well plate for subsequent ZIKV infection. In parallel, total RNA was extracted using Quick-RNA MiniPrep Plus kit (Zymo Research, #R1055). 500 ng of RNA was used to synthesize complementary DNA using qScript cDNA synthesis kit (Quanta, #101414–106). Samples were diluted tenfold and gene expression was analyzed by a CFX96 Touch Detection System (Bio-Rad) using FastStart SYBR Green Master Mix (Roche). See also Table S2 for shRNA sequences and primer pairs.

Quantitative PCR—Total cellular RNA was isolated using TRIzol reagent (Sigma-Aldrich), followed by RT into cDNA using the qScript cDNA Synthesis kit (Quanta BioSciences). Real-time PCR was performed using an Applied Biosystems 7500HT cycler using Taq-Man Universal PCR Master Mix (Thermofisher Scientific). See also Table S2 for primer pairs sequences.

NanoString nCounter Gene Expression—Total RNA was extracted from mock or ZIKV-infected GSC-brain cortical organoids using QIAGEN RNeasy Mini Plus kit according to manufacturer's instructions. 50ng of total RNA was then processed with the NanoString nCounter system (NanoString, Seattle, Washington, USA) per vendor instructions with Human Immunology Panel. Data export and normalization were performed using nSolver software (NanoString). Data was further analyzed using Rosalind On Ramp software.

Rosalind NanoString analysis methods—Data was analyzed by Rosalind (https://rosalind.onramp.bio/), with a HyperScale architecture developed by OnRamp BioInformatics, Inc. (San Diego, CA). Read Distribution percentages, violin plots, identity heatmaps, and sample MDS plots were generated as part of the QC step. The limma R library (Ritchie et al., 2015) was used to calculate fold changes and p values. Clustering of genes for the final heatmap of differentially expressed genes was done using the PAM (Partitioning Around Medoids) method using the fpc R library that takes into consideration of the direction and type of all signals on a pathway, the position, role and type of every gene, etc. Functional enrichment analysis of pathways, gene ontology, domain structure and other ontologies was performed using HOMER (Heinz et al., 2010). Several database sources were referenced for enrichment analysis, including Interpro (Mitchell et al., 2019), NCBI (Geer et al., 2010), KEGG6 (Kanehisa et al., 2017, 2019), MSigDB (Subramanian et al., 2005; Liberzon et al., 2011), REACTOME (Fabregat et al., 2018), WikiPathways (Slenter et al., 2018). Enrichment was calculated relative to a set of background genes relevant for the experiment. Additional gene enrichment is available from the following partner institutions: Advaita (http://advaitabio.com/ipathwayguide/; Draghici et al., 2007; Donato et al., 2013).

Western blotting—Cells were collected and lysed in RIPA buffer (50 mmol/L Tris-HCl, pH 7.5; 150 mmol/L NaCl; 0.5% NP-40; 50 mmol/L NaF with protease inhibitors) and incubated on ice for 30 minutes. Lysates were centrifuged at 14,000 rpm at 4°C for 10 minutes, and supernatant was collected. Protein concentration was determined using the Bradford assay (Bio-Rad Laboratories). Equal amounts of protein samples were mixed with SDS Laemmli loading buffer, boiled and electrophoresed using NuPAGE Bis-Tris Gels (Life Technologies), and then transferred onto PVDF membranes (Millipore). Blocking was performed for 45 minutes using TBS-T supplemented with 5% nonfat dry milk and blotting performed with primary antibodies at 4°C for 16 hours. Primary antibodies used were SOX2 antibody (R&D, #AF2018), OLIG2 antibody (Millipore, #MABN50), GFAP antibody (BD, #BDB610565), β-Actin antibody (Cell signaling, #4970), Integrin alpha V antibody (Abcam, ab124968), Integrin β5 antibody (R&D, AF3824), Integrin β3 antibody (Sigma-Aldrich, SAB4501586), Integrin alpha 6 antibody (Abcam, ab181551), Cleaved Caspase-3 antibody (Cell signaling, #9664) and GAPDH antibody (Abcam, ab9484).

***In silico* analysis—**mRNA data were obtained from The Cancer Genome Atlas (TCGA) GBM HG-U133A microarray dataset using the GlioVis web portal (Bowman et al., 2017). Expression of each gene was correlated with expression of SOX2. A “SOX2 positively correlated” gene set was defined by selecting genes with an $r > 0.4$ and the “SOX2 negatively correlated” gene set was defined by selecting genes with an $r < -0.4$. Gene sets were inputted into the Broad Institute online Gene Set Enrichment Analysis (GSEA) Tool (Mootha et al., 2003; Subramanian et al., 2005) (http://software.broadinstitute.org/gsea/index.jsp). The top enrichment pathways were visualized using a bar graph showing the $-\text{Log}_{10}$ of FDR corrected p value for the pathway enrichment. Gene set enrichment bubble plots were generated using the Bader Lab Enrichment Map (Merico et al., 2010) in cytoscape. Bubbles represent single gene sets that are enriched with lines demonstrating overlapping genes between enriched pathways. The borders of the circles represent the FDR corrected p value for each pathway.

ChIP-Seq and ChIP-PCR—Cells (5×10^6) per condition were collected, and 5 mg SOX2 antibody (R&D Systems, #AF2018-SP) or goat-IgG (R&D Systems, #AB-108-C) was used for the immunoprecipitation of the DNA protein immunocomplexes. ChIP was performed using the Millipore Magna ChIP (MAGNA0017) according to the manufacturer’s protocol. See also Table S3 for the purified DNA qPCR primer sets.

Three technical replicates were performed with SOX2 ChIP-PCR data presented as fold change relative to the non-specific antibody (goat-IgG). Stem and differentiated glioma cell ChIP-seq data were downloaded from GEO using accession number GSE54047. GBM primary tissue ChIP-seq data was accessed from GSE101148. Normal Brain primary tissue ChIP-seq data was accessed through the publicly available Roadmap Epigenomics (http://www.roadmapepigenomics.org/) and Encode Project web portals (https://www.encodeproject.org/). Data were viewed using IGV (http://software.broadinstitute.org/software/igv/).

Flow cytometry—Cell pellets were washed with PBS and blocked with 1% BSA in PBS for 30 minutes at room temperature and stained with anti-$\alpha_v\beta_5$ antibody (Millipore,

#MAB1961, 5 μg/mL in 1% BSA in PBS) and a fluorescently labeled secondary antibody (Thermofisher, #A21235, 1:1000). After the staining, the cells were incubated with PI (Sigma-Aldrich, #P4864, 1:1000), and flow cytometry was performed on BD LSRFortessa™. The levels of $\alpha_v\beta_5$ integrin were analyzed using the flow cytometry analysis program FlowJo (FlowJo, LLC).

Apoptosis assays—Apoptosis was assessed using the Dead Cell Apoptosis Kit with Annexin V Alexa Fluor 488 from Thermofisher (#V13241) according to the manufacturer's instructions. Samples were analyzed using flow cytometry on a BD LSR Fortessa Flow Cytometer.

CRISPR-Cas9 gRNA and cloning—The CRISPR design tool from the Broad Institute (https://portals.broadinstitute.org/gpp/public/analysis-tools/sgrna-design) was used to design the guide RNA (gRNA). Oligonucleotides were purchased from Thermofisher and were annealed and cloned into LentiCRISPR v2 plasmid, which was a gift from F. Zhang (Addgene plasmid 52961). 293FT cells were used to generate lentiviral particles through co-transfection of the packaging vectors pCMV-dR8.2 dvpr and pCI-VSVG using a standard calcium phosphate transfection method in Neurobasal complete media.

For knockout studies, GSC3565 cells were transduced with a CRISPR-Cas9 construct targeting integrins or a non-targeting control and selected for integration of the lentiviral construct by puromycin. Single cells were expanded *in vitro* to obtain clonal populations and knockout was confirmed by immunostaining and western blotting. Two clonal populations per sgRNA were subjected to parallel *in vitro* proliferation assays and *in vivo* survival assays. For *in vitro* studies, cells were plated in 96-well plates on Matrigel as above and maintained in standard serum-free media. For *in vivo* studies, cells were intracranially implanted into age-matched female NSG mice. Between five and six mice where used for each sgRNA construct. All mice were monitored daily until development of neurological signs, at which time they were euthanized, as described previously (Wang et al., 2018). See also Table S4 for the gRNA oligonucleotide sequences.

ZIKV *in vivo* inoculation experiments—The 4–6 weeks old female NSG mice (NOD.Cg-*Prkdc*^{scid} *Il2rg*^{tm1Wjl}/SzJl, #005557) were purchased from Jackson Laboratory. All animal experiments were approved by the Animal Experiment Committee of Laboratory Animal Center (Washington University, IACUC-20170066). For the ZIKV transformed NPCs *in vivo* study, NSG mice were inoculated intracranially with 10^3 FFU of ZIKA.HPAN or PRV at subventricular zone (SVZ). PBS injection was used as a control. For the tumor implantation survival study, groups of NSG mice were inoculated intracranially with 10^4 GSC3565. For P1F6 treatment, GSC3565 were incubated with $\alpha_v\beta_5$ antibody at 50 μg/ml for an hour in cold PBS. For ZIKV inoculation, 10^3 FFU of ZIKA.HPAN or PRV was mixed with GSCs before implantation *in vivo*. PBS injection was used as a control.

Histology—10 μm-thick sections of paraffin-embedded tissues were analyzed for hematoxylin and eosin (H&E; Thermofisher), Picro-Sirius Red (Sigma-Aldrich), and Masson's Trichrome (Diagnostic Biosystems) according to the manufacturer's instructions. 4 ×, 10 ×, and 20 × images were captured by AT2 Aperio Scan Scope. Image analysis was

performed by thresholding for positive staining and normalizing to total tissue area using ImageJ (NIH) and MetaMorph v7.7.0.0 (Molecular Devices) software.

TUNEL staining—Tissue sections were deparaffinized and permeabilized with proteinase K (25 μg/ml in 100 mM Tris·HCl). An *in situ* apoptotic cell death detection kit (TUNEL Assay Kit - HRP-DAB, Abcam) based on the TUNEL assay was used as per the manufacturer's instructions to detect apoptotic cells. The percentage of apoptotic nuclei per section was calculated by counting the total number of TUNEL-staining nuclei divided by the total number of hematoxylin-positive nuclei in 8–10 randomly selected fields at × 20 magnification.

Human induced pluripotent stem cells (iPSCs), NPCs and BCO generation —Human iPSCs cell lines obtained from healthy patients were generated as previously described (Marchetto et al., 2010; Chailangkarn et al., 2016), by reprogramming fibroblasts from healthy donors. The iPSC colonies were plated on Matrigel-coated (BD Biosciences) plates and maintained in mTESR media (Stem Cell Technologies). hiPSC-derived NPCs were obtained and maintained as previously described (Marchetto et al., 2010; Chailangkarn et al., 2016). The iPSCs lines maintained in mTESR media were switched to N2 media, DMEM/F12 media supplemented with 1x N2 NeuroPlex Serum-Free Supplement (Gemini) supplemented with the dual SMAD inhibitors 1 μM of dorsomorphin (Tocris) and 10 μM of SB431542 (Stemgent) daily, for 48 hours. After two days, colonies were scraped off and cultured under agitation (95 rpm) as embryoid bodies (EB) for seven days using N2 media with dorsomorphin and SB431542. Media was changed every other day. EBs were then plated on Matrigel-coated dishes and maintained in DMEM/F12 supplemented with 0.5x of N2 supplement, 0.5x Gem21 NeuroPlex Serum-Free Supplement (Gemini), 20 ng/ml basic fibroblast growth factor (bFGF, Life Technologies) and 1% penicillin/streptomycin (P/S). After seven days in culture, rosettes arising from the plated EBs were manually picked, gently dissociated with StemPro Accutase (Life Technologies) and plated onto poly-L-ornithine/Laminin-coated (Life Technologies) plates. NPCs were maintained in DMEM/F12 with 0.5x N2, 0.5x Gem21, 20 ng/ml bFGF and 1% P/S. The media was changed every other day. NPCs were split as soon as confluent using StemPro Accutase for 5 mininutes at 37°C, centrifuged and replated with NGF with a 1:3 ratio in poly-L-ornithine/Laminin-coated plates.

Human iPSC-derived cortical organoids were obtained as previously described by Paşca et al. (2015) with modifications (Thomas et al., 2017; Trujillo et al., 2019). Briefly, iPSC colonies were gently dissociated using Accutase in PBS (1:1) (Life Technologies). Cells were then transferred to 6-well plates and kept under suspension. For neural induction, media containing DMEM/F12, 15 mM HEPES, 1x Glutamax, 1x N2 NeuroPlex (Gemini), 1x MEM-NEAA, 1 μM dorsomorphin (R&D Systems), 10 μM SB431542 (Stemgent) and 100 U/ml penicillin-streptomycin was used for six days. NPCs proliferation was obtained in the presence of Neurobasal media supplemented with 2x Gem21 NeuroPlex, 1x NEAA, 1x Glutamax, 20 ng/ml bFGF (Life Technologies) for seven days followed by seven additional days with the same media supplemented with 20 ng/ml EGF (PeproTech). Finally, for neuronal maturation, Neurobasal media supplemented 2x Gem21 NeuroPlex, 1x NEAA, 1x

Glutamax, 10ng/mL of BDNF, 10ng/mL of GDNF, 10ng/mL of NT-3 (all from PeproTech), 200 μM L-ascorbic acid and 1mM dibutyryl-cAMP (Sigma-Aldrich) was used for seven days. The cells were kept in the same media thereafter in the absence of growth factors for neuronal maturation.

All the cell lines tested negative for mycoplasma contamination. All experiments were approved and performed in accordance with the Institutional Review Boards (IRB) and Embryonic Stem Cell Research Oversight (ESCRO) guidelines and regulations.

Generation of GFP-BCOs—The PGK-EGFP lentiviral vector construct was provided by Dr. Peter Yingxiao Wang's laboratory in UC San Diego. For virus production, HEK293T cells were transfected with Lipofectamine 2000, the virus was harvested and concentrated using PEG-it solution according to manufacturer's instructions (System Biosciences). A healthy control iPS line was then infected with the PGK-EGFP lentivirus and the $EGFP^+$ cells were sorted by FACS (Aria, BD Biosciences) and replated on Matrigel plates. The brain cortical organoids were then generated from the sorted iPS cells.

GSC-brain cortical organoid formation—10^2 to 10^5 3565, 387 or 1517 GFP-labeled GSCs were added per BCOs and allowed to proliferate. GFP-labeled GSCs were present inside brain cortical organoids as early as 24 hours post-addition. The experiments were conducted 2–3 weeks after adding GSCs onto the BCOs. Neurobasal media supplemented with 1X GEM21 (Gemini), 1% NEAA (Life Technologies), 1% Glutamax (Life Technologies) and 1% penicillin/streptomycin (Life Technologies) was used throughout the experiment.

GSC organoid formation—Between 1×10^5 or 2×10^5 of 3565, 387 or 1517 GSCs were put per well in a 24-well plate under constant agitation at 95 rpm at 37°C in Neurobasal media supplemented with 1X GEM21 (Gemini), 1% NEAA (Life Technologies), 1% Glutamax (Life Technologies) and 1% penicillin/streptomycin (Life Technologies). The organoids started forming as early as 2 days after being put in suspension but were allowed to grow for 2–4 weeks before performing subsequent experiments.

GBM organoid and BCOs *in vitro* ZIKV infection—GSC-BCOs and GSC organoids were infected with H/PAN/2016/BEI-259634, Panama 2016 and PRVABC59, Puerto Rico 2015 ZIKV strains for 2 hours at 37°C at MOI of 5 FFU/cell and then the media containing the virus were removed and fresh media were added, Neurobasal media supplemented with 1X GEM21 (Gemini), 1% NEAA (Life Technologies), 1% Glutamax (Life Technologies) and 1% penicillin/streptomycin (Life Technologies).

Anti-integrin $\alpha_v\beta_5$ antibody treatment of GBM organoids—2- to 4-weeks-old GSC organoids were incubated with 50 μg/ml of the integrin $\alpha_v\beta_5$ antibody for 2–4 hours, then infected with PRVABC59 ZIKV strain for 2 hours at 37°C at an MOI of 5 FFU/cell. The media was then removed and fresh media containing 50 μg/ml of integrin $\alpha_v\beta_5$ antibody was added. The integrin $\alpha_v\beta_5$ antibody was added twice a week and GSC organoids were monitored for a month.

Image analysis—To calculate the integrated density of GFP in GSC-brain cortical organoids, ImageJ software was used. Briefly, the channels were split and the integrated density of the GFP channel was measured by the software.

Statistical analysis—All statistical analysis was performed using Prism 7.0 software (GraphPad). The number of animals and replicate experiments is specified in each figure legend. Sample size is similar to those reported in previous publications (Wang et al., 2017a). All grouped data were presented as mean ± SEM as indicated in the figure legends. Student's t test, one-way ANOVA with Tukey multiple comparison correction, and two-way ANOVA with the Bonferroni multiple comparison test were used to assess the significance of differences between groups. These tests were performed when the sample size was large enough to assume that the means were normally distributed or that the distribution of residuals was normal. For groups being statistically compared, variances in data were similar. For animal survival analysis, Kaplan-Meier curves were generated and the Log-rank test was performed to assess statistical significance between groups.

DATA AND CODE AVAILABILITY

Correlation between gene expression and patient survival was performed through analysis of The Cancer Genome Atlas (TCGA) and brain tumor datasets downloaded from the TCGA data portal (http://gliovis.bioinfo.cnio.es/) or NCBI GEO database. Raw data from enhancer profiling of primary glioma tissues were deposited at GSE101148. ChIP-seq data from Suvà et al. (2014) were accessed from the NCBI GEO database at GSE54792 and GSE17312.

Supplementary Material

Refer to Web version on PubMed Central for supplementary material.

ACKNOWLEDGMENTS

We thank Drs. Peter Yingxiao Wang and Hsin-Hung Lin (UC, San Diego) for the PGK-EGFP lentiviral vector and Dr. Elsa Molina (UC, San Diego Stem Cell Genomics Core) for technical assistance with experiments using the NanoString nCounter Sprint. We also acknowledge access and use of the UCSD Screening Core to perform part of the experiments presented in this manuscript. This work was made possible in part by CIRM Major Facilities grant FA1-00607 (to the Sanford Consortium for Regenerative Medicine). P.M. has an International Rett Syndrome Foundation (IRSF) mentored training fellowship. A.R.M. is supported by the California Institute for Regenerative Medicine (DISC2-09649). These studies were supported by the NIH through CA217065 (to R.C.G.); CA217066 (to B.C.P.); CA203101 (to L.J.Y.K.); CA159859 and CA199376 (to S.S.); NS097649-01 and CA240953-01 (to C.C.C.); NS096368 (to R.J.W.-R.); R01DK103901 and R01AA027065 (to H.H.); MH107367 and N5105969 (to A.R.M.); CA045726 and CA050286 (to D.A.C.); and CA197718, CA154130, CA169117, CA171652, NS087913, and NS089272 (to J.N.R.).

REFERENCES

Allen C, Opyrchal M, Aderca I, Schroeder MA, Sarkaria JN, Domingo E, Federspiel MJ, and Galanis E (2013). Oncolytic measles virus strains have significant antitumor activity against glioma stem cells. Gene Ther. 20, 444–449. [PubMed: 22914495]

Bach P, Abel T, Hoffmann C, Gal Z, Braun G, Voelker I, Ball CR, Johnston IC, Lauer UM, Herold-Mende C, et al. (2013). Specific elimination of CD133+ tumor cells with targeted oncolytic measles virus. Cancer Res. 73, 865–874. [PubMed: 23293278]

Bao S, Wu Q, McLendon RE, Hao Y, Shi Q, Hjelmeland AB, Dewhirst MW, Bigner DD, and Rich JN (2006a). Glioma stem cells promote radio-resistance by preferential activation of the DNA damage response. Nature 444, 756–760. [PubMed: 17051156]

Bao S, Wu Q, Sathornsumetee S, Hao Y, Li Z, Hjelmeland AB, Shi Q, McLendon RE, Bigner DD, and Rich JN (2006b). Stem cell-like glioma cells promote tumor angiogenesis through vascular endothelial growth factor. Cancer Res. 66, 7843–7848. [PubMed: 16912155]

Boonnak K, Slike BM, Burgess TH, Mason RM, Wu SJ, Sun P, Porter K, Rudiman IF, Yuwono D, Puthavathana P, and Marovich MA (2008). Role of dendritic cells in antibody-dependent enhancement of dengue virus infection. J. Virol 82, 3939–3951. [PubMed: 18272578]

Bowman RL, Wang Q, Carro A, Verhaak RG, and Squatrito M (2017). GlioVis data portal for visualization and analysis of brain tumor expression datasets. Neuro Oncol. 19, 139–141. [PubMed: 28031383]

Brinton MA (2013). Replication cycle and molecular biology of the West Nile virus. Viruses 6, 13–53. [PubMed: 24378320]

Buetow MP, Buetow PC, and Smirniotopoulos JG (1991). Typical, atypical, and misleading features in meningioma. Radiographics 11, 1087–1106. [PubMed: 1749851]

Chailangkarn T, Trujillo CA, Freitas BC, Hrvoj-Mihic B, Herai RH, Yu DX, Brown TT, Marchetto MC, Bardy C, McHenry L, et al. (2016). A human neurodevelopmental model for Williams syndrome. Nature 536, 338–343. [PubMed: 27509850]

Chen J, Yang YF, Yang Y, Zou P, Chen J, He Y, Shui SL, Cui YR, Bai R, Liang YJ, et al. (2018a). AXL promotes Zika virus infection in astrocytes by antagonizing type I interferon signalling. Nat. Microbiol 3, 302–309. [PubMed: 29379210]

Chen Q, Wu J, Ye Q, Ma F, Zhu Q, Wu Y, Shan C, Xie X, Li D, Zhan X, et al. (2018b). Treatment of Human Glioblastoma with a Live Attenuated Zika Virus Vaccine Candidate. MBio 9, e01683–e18. [PubMed: 30228241]

Chu JJH, and Ng ML (2004). Interaction of West Nile virus with alpha v beta 3 integrin mediates virus entry into cells. J. Biol. Chem 279, 54533–54541. [PubMed: 15475343]

Cosset É, Ilmjärv S, Dutoit V, Elliott K, von Schalscha T, Camargo MF, Reiss A, Moroishi T, Seguin L, Gomez G, et al. (2017). Glut3 Addiction Is a Druggable Vulnerability for a Molecularly Defined Subpopulation of Glioblastoma. Cancer Cell 32, 856–868.e5. [PubMed: 29198914]

Darmanis S, Sloan SA, Croote D, Mignardi M, Chernikova S, Samghababi P, Zhang Y, Neff N, Kowarsky M, Caneda C, et al. (2017). Single-Cell RNA-Seq Analysis of Infiltrating Neoplastic Cells at the Migrating Front of Human Glioblastoma. Cell Reports 21, 1399–1410. [PubMed: 29091775]

Desgrosellier JS, and Cheresh DA (2010). Integrins in cancer: biological implications and therapeutic opportunities. Nat. Rev. Cancer 10, 9–22. [PubMed: 20029421]

Donato M, Xu Z, Tomoiaga A, Granneman JG, Mackenzie RG, Bao R, Than NG, Westfall PH, Romero R, and Draghici S (2013). Analysis and correction of crosstalk effects in pathway analysis. Genome Res. 23, 1885–1893. [PubMed: 23934932]

Draghici S, Khatri P, Tarca AL, Amin K, Done A, Voichita C, Georgescu C, and Romero R (2007). A systems biology approach for pathway level analysis. Genome Res. 17, 1537–1745. [PubMed: 17785539]

Drost J, and Clevers H (2018). Organoids in cancer research. Nat. Rev. Cancer 18, 407–418. [PubMed: 29692415]

Fabregat A, Jupe S, Matthews L, Sidiropoulos K, Gillespie M, Garapati P, Haw R, Jassal B, Korninger F, May B, et al. (2018). The Reactome Pathway Knowledgebase. Nucleic Acids Res. 46, D649–D655. [PubMed: 29145629]

Fan W, Qian P, Wang D, Zhi X, Wei Y, Chen H, and Li X (2017). Integrin αvβ3 promotes infection by Japanese encephalitis virus. Res. Vet. Sci 111, 67–74. [PubMed: 28043010]

Foo SS, Chen W, Chan Y, Bowman JW, Chang LC, Choi Y, Yoo JS, Ge J, Cheng G, Bonnin A, et al. (2017). Asian Zika virus strains target $CD14^{+}$ blood monocytes and induce M2-skewed immunosuppression during pregnancy. Nat. Microbiol 2, 1558–1570. [PubMed: 28827581]

Foreman PM, Friedman GK, Cassady KA, and Markert JM (2017). Oncolytic Virotherapy for the Treatment of Malignant Glioma. Neurotherapeutics 14, 333–344. [PubMed: 28265902]

Gangemi RMR, Griffero F, Marubbi D, Perera M, Capra MC, Malatesta P, Ravetti GL, Zona GL, Daga A, and Corte G (2009). SOX2 Silencing in Glioblastoma Tumor-Initiating Cells Causes Stop of Proliferation and Loss of Tumorigenicity. Stem Cells 27, 40–48. [PubMed: 18948646]

Garcez PP, Loiola EC, Madeiro da Costa R, Higa LM, Trindade P, Delvecchio R, Nascimento JM, Brindeiro R, Tanuri A, and Rehen SK (2016). Zika virus impairs growth in human neurospheres and brain organoids. Science 352, 816–818. [PubMed: 27064148]

Geer LY, Marchler-Bauer A, Geer RC, Han L, He J, He S, Liu C, Shi W, and Bryant SH (2010). The NCBI BioSystems database. Nucleic Acids Res. 38, D492–D496. [PubMed: 19854944]

Heinz S, Benner C, Spann N, Bertolino E, Lin YC, Laslo P, Cheng JX, Murre C, Singh H, and Glass CK (2010). Simple combinations of lineage-determining transcription factors prime cis-regulatory elements required for macrophage and B cell identities. Mol. Cell 38, 576–589. [PubMed: 20513432]

Heymann DL, Hodgson A, Sall AA, Freedman DO, Staples JE, Althabe F, Baruah K, Mahmud G, Kandun N, Vasconcelos PF, et al. (2016). Zika virus and microcephaly: why is this situation a PHEIC? Lancet 387, 719–721. [PubMed: 26876373]

Hu Y, and Smyth GK (2009). ELDA: Extreme limiting dilution analysis for comparing depleted and enriched populations in stem cell and other assays. J. Immunol. Methods 347, 70–78. [PubMed: 19567251]

Hubert CG, Rivera M, Spangler LC, Wu Q, Mack SC, Prager BC, Couce M, McLendon RE, Sloan AE, and Rich JN (2016). A three-dimensional organoid culture system derived from human glioblastomas recapitulates the hypoxic gradients and cancer stem cell heterogeneity of tumors found in vivo. Cancer Res. 76, 2465–2477. [PubMed: 26896279]

Ianevski A, He l., Aittokallio T, and Tang J (2017). SynergyFinder: a web application for analyzing drug combination dose–response matrix data. Bioinformatics 33, 2413–2415. [PubMed: 28379339]

Josupeit R, Bender S, Kern S, Leuchs B, Hielscher T, Herold-Mende C, Schlehofer JR, Dinsart C, Witt O, Rommelaere J, and Lacroix J (2016). Pediatric and Adult High-Grade Glioma Stem Cell Culture Models Are Permissive to Lytic Infection with Parvovirus H-1. Viruses 8, E138. [PubMed: 27213425]

Kaid C, Goulart E, Caires-Júnior LC, Araujo BHS, Soares-Schanoski A, Bueno HMS, Telles-Silva KA, Astray RM, Assoni AF, Júnior AFR, et al. (2018). Zika virus selectively kills aggressive human embryonal CNS tumor cells in vitro and in vivo. Cancer Res. 78, 3363–3374. [PubMed: 29700002]

Kanehisa M, Furumichi M, Tanabe M, Sato Y, and Morishima K (2017). KEGG: new perspectives on genomes, pathways, diseases and drugs. Nucleic Acids Res. 45, D353–D361. [PubMed: 27899662]

Kanehisa M, Sato Y, Furumichi M, Morishima K, and Tanabe M (2019). New approach for understanding genome variations in KEGG. Nucleic Acids Res. 47, D590–D595. [PubMed: 30321428]

Lathia JD, Gallagher J, Heddleston JM, Wang J, Eyler CE, Macswords J, Wu Q, Vasanji A, McLendon RE, Hjelmeland AB, and Rich JN (2010). Integrin alpha 6 regulates glioblastoma stem cells. Cell Stem Cell 6, 421–432. [PubMed: 20452317]

Lazear HM, Govero J, Smith AM, Platt DJ, Fernandez E, Miner JJ, and Diamond MS (2016). A Mouse Model of Zika Virus Pathogenesis. Cell Host Microbe 19, 720–730. [PubMed: 27066744]

Li C, Xu D, Ye Q, Hong S, Jiang Y, Liu X, Zhang N, Shi L, Qin CF, and Xu Z (2016). Zika Virus Disrupts Neural Progenitor Development and Leads to Microcephaly in Mice. Cell Stem Cell 19, 120–126. [PubMed: 27179424]

Liberzon A, Subramanian A, Pinchback R, Thorvaldsdóttir H, Tamayo P, and Mesirov JP (2011). Molecular signatures database (MSigDB) 3.0. Bioinformatics 27, 1739–1740. [PubMed: 21546393]

Liu F, Hon GC, Villa GR, Turner KM, Ikegami S, Yang H, Ye Z, Li B, Kuan S, Lee AY, et al. (2015). EGFR Mutation Promotes Glioblastoma through Epigenome and Transcription Factor Network Remodeling. Mol. Cell 60, 307–318. [PubMed: 26455392]

Love MI, Huber W, and Anders S (2014). Moderated estimation of fold change and dispersion for RNA-seq data with DESeq2. Genome Biology 15, 550. [PubMed: 25516281]

Mack SC, Pajtler KW, Chavez L, Okonechnikov K, Bertrand KC, Wang X, Erkek S, Federation A, Song A, Lee C, et al. (2018). Therapeutic targeting of ependymoma as informed by oncogenic enhancer profiling. Nature 553, 101–105. [PubMed: 29258295]

Mack SC, Singh I, Wang X, Hirsch R, Wu Q, Villagomez R, Bernatchez JA, Zhu Z, Gimple RC, Kim LJY, et al. (2019). Chromatin landscapes reveal developmentally encoded transcriptional states that define human glioblastoma. J. Exp. Med 216, 1071–1090. [PubMed: 30948495]

Marchetto MCN, Carromeu C, Acab A, Yu D, Yeo GW, Mu Y, Chen G, Gage FH, and Muotri AR (2010). A model for neural development and treatment of Rett syndrome using human induced pluripotent stem cells. Cell 143, 527–539. [PubMed: 21074045]

Medigeshi GR, Hirsch AJ, Streblow DN, Nikolich-Zugich J, and Nelson JA (2008). West Nile Virus Entry Requires Cholesterol-Rich Membrane Microdomains and Is Independent of alphavbeta3 Integrin. J. Virol 82, 5212–5219. [PubMed: 18385233]

Meertens L, Labeau A, Dejarnac O, Cipriani S, Sinigaglia L, Bonnet-Madin L, Le Charpentier T, Hafirassou ML, Zamborlini A, Cao-Lormeau VM, et al. (2017). Axl Mediates ZIKA Virus Entry in Human Glial Cells and Modulates Innate Immune Responses. Cell Rep. 18, 324–333. [PubMed: 28076778]

Merico D, Isserlin R, Stueker O, Emili A, and Bader GD (2010). Enrichment Map: A Network-Based Method for Gene-Set Enrichment Visualization and Interpretation. PLoS ONE 5, e13984. [PubMed: 21085593]

Mesci P, Macia A, LaRock CN, Tejwani L, Fernandes IR, Suarez NA, de A Zanotto PM, Beltrão-Braga PCB, Nizet V, and Muotri AR (2018). Modeling neuro-immune interactions during Zika virus infection. Hum. Mol. Genet 27, 41–52. [PubMed: 29048558]

Michlmayr D, Andrade P, Gonzalez K, Balmaseda A, and Harris E (2017). $CD14^{+}CD16^{+}$ monocytes are the main target of Zika virus infection in peripheral blood mononuclear cells in a paediatric study in Nicaragua. Nat. Microbiol 2, 1462–1470. [PubMed: 28970482]

Miner JJ, Cao B, Govero J, Smith AM, Fernandez E, Cabrera OH, Garber C, Noll M, Klein RS, Noguchi KK, et al. (2016). Zika Virus Infection during Pregnancy in Mice Causes Placental Damage and Fetal Demise. Cell 165, 1081–1091. [PubMed: 27180225]

Mitchell AL, Attwood TK, Babbitt PC, Blum M, Bork P, Bridge A, Brown SD, Chang HY, El-Gebali S, Fraser MI, et al. (2019). InterPro in 2019: improving coverage, classification and access to protein sequence annotations. Nucleic Acids Res. 47, D351–D360. [PubMed: 30398656]

Milde T, Kleber S, Korshunov A, Witt H, Hielscher T, Koch P, Kopp HG, Jugold M, Deubzer HE, Oehme I, et al. (2011). A novel human high-risk ependymoma stem cell model reveals the differentiation-inducing potential of the histone deacetylase inhibitor Vorinostat. Acta Neuropathol. 122, 637–650. [PubMed: 21863243]

Mootha VK, Lindgren CM, Eriksson KF, Subramanian A, Sihag S, Lehar J, Puigserver P, Carlsson E, Ridderstråle M, Laurila E, et al. (2003). PGC-1α-responsive genes involved in oxidative phosphorylation are coordinately downregulated in human diabetes. Nat. Genet 34, 267–273. [PubMed: 12808457]

Nowakowski TJ, Pollen AA, Di Lullo E, Sandoval-Espinosa C, Bershteyn M, and Kriegstein AR (2016). Expression Analysis Highlights AXL as a Candidate Zika Virus Entry Receptor in Neural Stem Cells. Cell Stem Cell 18, 591–596. [PubMed: 27038591]

Ogawa J, Pao GM, Shokhirev MN, and Verma IM (2018). Glioblastoma Model Using Human Cerebral Organoids. Cell Rep. 23, 1220–1229. [PubMed: 29694897]

Oh Y, Zhang F, Wang Y, Lee EM, Choi IY, Lim H, Mirakhori F, Li R, Huang L, Xu T, et al. (2017). Zika virus directly infects peripheral neurons and induces cell death. Nat. Neurosci 20, 1209–1212. [PubMed: 28758997]

Oliveira Melo AS, Malinger G, Ximenes R, Szejnfeld PO, Alves Sampaio S, and Bispo de Filippis AM (2016). Zika virus intrauterine infection causes fetal brain abnormality and microcephaly: tip of the iceberg? Ultrasound Obstet. Gynecol 47, 6–7. [PubMed: 26731034]

Paşca AM, Sloan SA, Clarke LE, Tian Y, Makinson CD, Huber N, Kim CH, Park JY, O'Rourke NA, Nguyen KD, et al. (2015). Functional cortical neurons and astrocytes from human pluripotent stem cells in 3D culture. Nat. Methods 12, 671–678. [PubMed: 26005811]

Petersen E, Wilson ME, Touch S, McCloskey B, Mwaba P, Bates M, Dar O, Mattes F, Kidd M, Ippolito G, et al. (2016). Rapid Spread of Zika Virus in The Americas–Implications for Public Health Preparedness for Mass Gatherings at the 2016 Brazil Olympic Games. Int. J. Infect. Dis 44, 11–15. [PubMed: 26854199]

Poirot L, Philip B, Schiffer-Mannioui C, Le Clerre D, Chion-Sotinel I, Derniame S, Potrel P, Bas C, Lemaire L, Galetto R, et al. (2015). Multiplex Genome-Edited T-cell Manufacturing Platform for "Off-the-Shelf" Adoptive T-cell Immunotherapies. Cancer Res. 75, 3853–3864. [PubMed: 26183927]

Pollen AA, Nowakowski TJ, Chen J, Retallack H, Sandoval-Espinosa C, Nicholas CR, Shuga J, Liu SJ, Oldham MC, Diaz A, et al. (2015). Molecular Identity of Human Outer Radial Glia during Cortical Development. Cell 163, 55–67. [PubMed: 26406371]

Qian X, Nguyen HN, Song MM, Hadiono C, Ogden SC, Hammack C, Yao B, Hamersky GR, Jacob F, Zhong C, et al. (2016). Brain-Region-Specific Organoids Using Mini-bioreactors for Modeling ZIKV Exposure. Cell 165, 1238–1254. [PubMed: 27118425]

Quinlan AR, and Hall IM (2010). BEDTools: a flexible suite of utilities for comparing genomic features. Bioinformatics 26, 841–842. [PubMed: 20110278]

Ramírez F, Ryan DP, Grüning BA, Bhardwaj V, Kilpert F, Richter AS, Heyne S, Dundar F, and Manke T (2016). deepTools2: a next generation web server for deep-sequencing data analysis. Nucleic Acids Res. 44, W160–W165. [PubMed: 27079975]

Reich M, Liefeld T, Gould J, Lerner J, Tamayo P, and Mesirov JP (2006). GenePattern 2.0. Nat. Genet 38, 500–501. [PubMed: 16642009]

Retallack H, Di Lullo E, Arias C, Knopp KA, Laurie MT, Sandoval-Espinosa C, Mancia Leon WR, Krencik R, Ullian EM, Spatazza J, et al. (2016). Zika virus cell tropism in the developing human brain and inhibition by azithromycin. Proc. Natl. Acad. Sci. USA 113, 14408–14413. [PubMed: 27911847]

Ritchie ME, Phipson B, Wu D, Hu Y, Law CW, Shi W, and Smyth GK (2015). limma powers differential expression analyses for RNA-sequencing and microarray studies. Nucleic Acids Res. 43, e47. [PubMed: 25605792]

Robinson JT, Thorvaldsdóttir H, Winckler W, Guttman M, Lander ES, Getz G, and Mesirov JP (2011). Integrative genomics viewer. Nat. Biotechnol 29, 24–26. [PubMed: 21221095]

Russell SJ, Peng KW, and Bell JC (2012). Oncolytic virotherapy. Nat. Biotechnol 30, 658–670. [PubMed: 22781695]

Sarkar A, and Hochedlinger K (2013). The sox family of transcription factors: versatile regulators of stem and progenitor cell fate. Cell Stem Cell 12, 15–30. [PubMed: 23290134]

Schafer ST, Paquola ACM, Stern S, Gosselin D, Ku M, Pena M, Kuret TJM, Liyanage M, Mansour AA, Jaeger BN, Marchetto MC, Glass CK, Mertens J, and Gage FH (2019). Pathological priming causes developmental gene network heterochronicity in autistic subject-derived neurons. Nat. Neurosci 22, 243–255. [PubMed: 30617258]

Schindelin J, Arganda-Carreras I, Frise E, Kaynig V, Longair M, Pietzsch T, Preibisch S, Rueden C, Saalfeld S, Schmid B, et al. (2012). Fiji: an open-source platform for biological-image analysis. Nat. Methods 9, 676–682. [PubMed: 22743772]

Schmidt K, Keller M, Bader BL, Korytář T, Finke S, Ziegler U, and Groschup MH (2013). Integrins modulate the infection efficiency of West Nile virus into cells. J. Gen. Virol 94, 1723–1733. [PubMed: 23658209]

Schuler-Faccini L, Ribeiro EM, Feitosa IM, Horovitz DD, Cavalcanti DP, Pessoa A, Doriqui MJ, Neri JI, Neto JM, Wanderley HY, et al. ; Brazilian Medical Genetics Society–Zika Embryopathy Task Force (2016). Possible Association Between Zika Virus Infection and Microcephaly - Brazil, 2015. MMWR Morb. Mortal. Wkly. Rep 65, 59–62. [PubMed: 26820244]

Seguin L, Kato S, Franovic A, Camargo MF, Lesperance J, Elliott KC, Yebra M, Mielgo A, Lowy AM, Husain H, et al. (2014). An integrin β_3-KRAS-RalB complex drives tumour stemness and resistance to EGFR inhibition. Nat. Cell Biol 16, 457–468. [PubMed: 24747441]

Seguin L, Camargo MF, Wettersten HI, Kato S, Desgrosellier JS, von Schalscha T, Elliott KC, Cosset E, Lesperance J, Weis SM, and Cheresh DA (2017). Galectin-3, a Druggable Vulnerability for KRAS-Addicted Cancers. Cancer Discov. 7, 1464–1479. [PubMed: 28893801]

Shannon P, Markiel A, Ozier O, Baliga NS, Wang JT, Ramage D, Amin N, Schwikowski B, and Ideker T (2003). Cytoscape: a software environment for integrated models of biomolecular interaction networks. Genome Res. 13, 2498–2504. [PubMed: 14597658]

Singh SK, Clarke ID, Terasaki M, Bonn VE, Hawkins C, Squire J, and Dirks PB (2003). Identification of a cancer stem cell in human brain tumors. Cancer Res. 63, 5821–5828. [PubMed: 14522905]

Slenter DN, Kutmon M, Hanspers K, Riutta A, Windsor J, Nunes N, Mélius J, Cirillo E, Coort SL, Digles D, et al. (2018). WikiPathways: a multi-faceted pathway database bridging metabolomics to other omics research. Nucleic Acids Res. 46, D661–D667. [PubMed: 29136241]

Soneson C, Love MI, and Robinson MD (2016). Differential analyses for RNA-seq: transcript-level estimates improve gene-level inferences. F1000Res 4, 1521.

Souza BSF, Sampaio GL, Pereira CS, Campos GS, Sardi SI, Freitas LA, Figueira CP, Paredes BD, Nonaka CK, Azevedo CM, et al. (2016). Zika virus infection induces mitosis abnormalities and apoptotic cell death of human neural progenitor cells. Sci. Rep 6, 39775. [PubMed: 28008958]

Stupp R, Mason WP, van den Bent MJ, Weller M, Fisher B, Taphoorn MJ, Belanger K, Brandes AA, Marosi C, Bogdahn U, et al. (2005). Radiotherapy plus Concomitant and Adjuvant Temozolomide for Glioblastoma. N. Engl. J. Med 352, 987–996. [PubMed: 15758009]

Subramanian A, Tamayo P, Mootha VK, Mukherjee S, Ebert BL, Gillette MA, Paulovich A, Pomeroy SL, Golub TR, Lander ES, and Mesirov JP (2005). Gene set enrichment analysis: A knowledge-based approach for interpreting genome-wide expression profiles. Proc. Natl. Acad. Sci. USA 102, 15545–15550. [PubMed: 16199517]

Suvà ML, Rheinbay E, Gillespie SM, Patel AP, Wakimoto H, Rabkin SD, Riggi N, Chi AS, Cahill DP, Nahed BV, et al. (2014). Reconstructing and reprogramming the tumor-propagating potential of glioblastoma stem-like cells. Cell 157, 580–594. [PubMed: 24726434]

Tang H, Hammack C, Ogden SC, Wen Z, Qian X, Li Y, Yao B, Shin J, Zhang F, Lee EM, et al. (2016). Zika Virus Infects Human Cortical Neural Progenitors and Attenuates Their Growth. Cell Stem Cell 18, 587–590. [PubMed: 26952870]

Tang Z, Li C, Kang B, Gao G, Li C, and Zhang Z (2017). GEPIA: a web server for cancer and normal gene expression profiling and interactive analyses. Nucleic Acids Res. 45, W98–W102. [PubMed: 28407145]

Thomas CA, Tejwani L, Trujillo CA, Negraes PD, Herai RH, Mesci P, Macia A, Crow YJ, and Muotri AR (2017).). Modeling of TREX1-Dependent Autoimmune Disease using Human Stem Cells Highlights L1 Accumulation as a Source of Neuroinflammation. Cell Stem Cell 21, 319–331.e8. [PubMed: 28803918]

Thorvaldsdottir H, Robinson JT, and Mesirov JP (2013). Integrative Genomics Viewer (IGV): high-performance genomic data visualization and exploration. Brief. Bioinform 14, 178–192. [PubMed: 22517427]

Trujillo CA, Gao R, Negraes PD, Gu J, Buchanan J, Preissl S, Wang A, Wu W, Haddad GG, Chaim IA, et al. (2019). Complex Oscillatory Waves Emerging from Cortical Organoids Model Early Human Brain Network Development. Cell Stem Cell 25, 558–569.e7. [PubMed: 31474560]

Wakimoto H, Kesari S, Farrell CJ, Curry WT Jr., Zaupa C, Aghi M, Kuroda T, Stemmer-Rachamimov A, Shah K, Liu TC, et al. (2009). Human glioblastoma-derived cancer stem cells: establishment of invasive glioma models and treatment with oncolytic herpes simplex virus vectors. Cancer Res. 69, 3472–3481. [PubMed: 19351838]

Wang X, Huang Z, Wu Q, Prager BC, Mack SC, Yang K, Kim LJY, Gimple RC, Shi Y, Lai S, et al. (2017a). MYC-regulated mevalonate metabolism maintains brain tumor–initiating cells. Cancer Res. 77, 4947–4960. [PubMed: 28729418]

Wang X, Yang K, Xie Q, Wu Q, Mack SC, Shi Y, Kim LJY, Prager BC, Flavahan WA, Liu X, et al. (2017b). Purine synthesis promotes maintenance of brain tumor initiating cells in glioma. Nat. Neurosci 20, 661–673. [PubMed: 28346452]

Wang X, Prager BC, Wu Q, Kim LJY, Gimple RC, Shi Y, Yang K, Morton AR, Zhou W, Zhu Z, et al. (2018). Reciprocal Signaling between Glioblastoma Stem Cells and Differentiated Tumor Cells Promotes Malignant Progression. Cell Stem Cell 22, 514–528.e5. [PubMed: 29625067]

Wells MF, Salick MR, Wiskow O, Ho DJ, Worringer KA, Ihry RJ, Kommineni S, Bilican B, Klim JR, Hill EJ, et al. (2016). Genetic Ablation of AXL Does Not Protect Human Neural Progenitor Cells and Cerebral Organoids from Zika Virus Infection. Cell Stem Cell 19, 703–708. [PubMed: 27912091]

Wickham TJ, Mathias P, Cheresh DA, and Nemerow GR (1993). Integrins α v β 3 and α v β 5 promote adenovirus internalization but not virus attachment. Cell 73, 309–319. [PubMed: 8477447]

Wu A, Wei J, Kong LY, Wang Y, Priebe W, Qiao W, Sawaya R, and Heimberger AB (2010). Glioma cancer stem cells induce immunosuppressive macrophages/microglia. Neuro-oncol. 12, 1113–1125. [PubMed: 20667896]

Wu X, Dao Thi VL, Huang Y, Billerbeck E, Saha D, Hoffmann HH, Wang Y, Silva LAV, Sarbanes S, Sun T, et al. (2018). Intrinsic Immunity Shapes Viral Resistance of Stem Cells. Cell 172, 423–438.e25. [PubMed: 29249360]

Zemp FJ, Lun X, McKenzie BA, Zhou H, Maxwell L, Sun B, Kelly JJ, Stechishin O, Luchman A, Weiss S, et al. (2013). Treating brain tumor-initiating cells using a combination of myxoma virus and rapamycin. Neuro. Oncol 15, 904–920. [PubMed: 23585629]

Zhou J, Li C, Sachs N, Chiu MC, Wong BH, Chu H, Poon VK, Wang D, Zhao X, Wen L, et al. (2018). Differentiated human airway organoids to assess infectivity of emerging influenza virus. Proc. Natl. Acad. Sci. USA 115, 6822–6827. [PubMed: 29891677]

Zhu Z, Gorman MJ, McKenzie LD, Chai JN, Hubert CG, Prager BC, Fernandez E, Richner JM, Zhang R, Shan C, et al. (2017). Zika virus has oncolytic activity against glioblastoma stem cells. J. Exp. Med 214, 2843–2857. [PubMed: 28874392]

Highlights

- ZIKV preferentially infects glioblastoma stem cells (GSCs) rather than neural precursor cells
- ZIKV kills SOX2+ cells from a diverse array of malignant brain tumors
- SOX2 determines susceptibility to ZIKV infection with reduced antiviral responses
- Integrin $\alpha_v\beta_5$ is a GSC marker and promotes Zika virus infection of GSCs

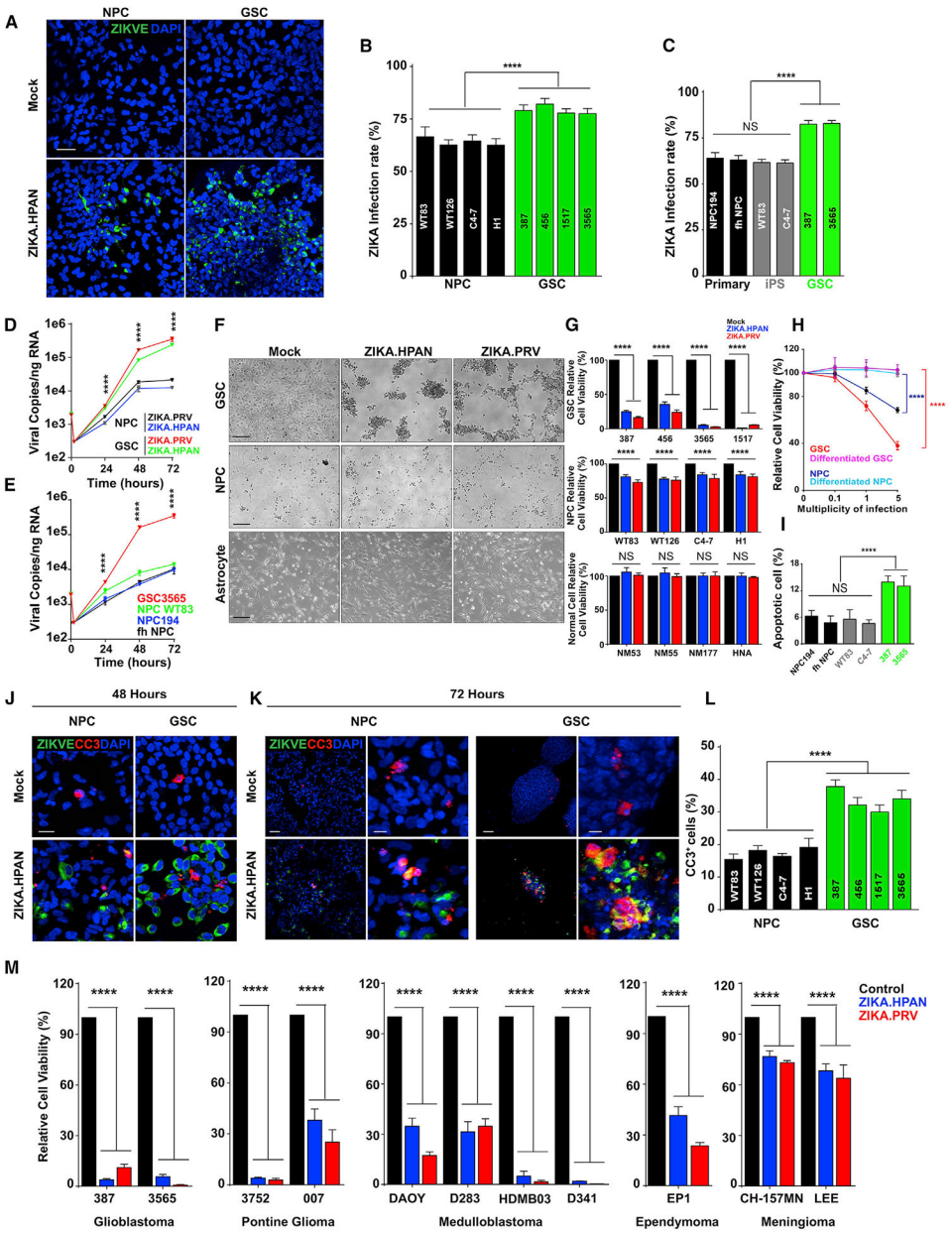

Figure 1. Zika Virus (ZIKV) Infects and Kills GBM Stem Cells (GSCs) More Efficiently Than Neural Precursor Cells (NPCs)

(A) Representative immunostaining for ZIKV envelope protein (ZIKV-E, green) and DAPI (blue) of GSCs and forebrain-specific NPCs 48 h post-infection (p.i.) with ZIKV. Scale bar, 50 μm.

(B) Quantification of infection efficiency in four GSC and NPC lines 48 h p.i. with ZIKV.

(C) Quantification of ZIKV^{+} cells in a panel of human GSCs and NPCs.

(D) Kinetics of viral RNA copies p.i. with ZIKV by measuring viral RNA copies by qRT-PCR in NPC C4–7 and GSC3565.

(E) ZIKV infection efficiency of GSCs and NPCs was measured by direct measurement of viral RNA copies.

(F) Representative bright-field images 5 days p.i. with ZIKV for GSCs, NPCs, and primary astrocytes. Scale bars, 50 μm.

(G) Cell viability normalized to day 5 mock, as measured 5 days p.i. with ZIKV for GSCs, NPCs, and primary astrocytes.

(H) GSCs (GSC3565), differentiated GSCs, NPCs (NPC C4–7), and differentiated NPCs were assayed for cell viability 72 h p.i. with ZIKV.

(I) Apoptosis of GSCs (387, 3565) and primary (NPC194, fetal human [fh] NPC) or iPSC-derived NPCs (WT83, C4–7) p.i. with ZIKV was measured by cleaved caspase-3 (CC3) staining.

(J) Representative immunostaining for ZIKV-E (green), CC3 (red), and DAPI (blue) of GSCs and forebrain-specific NPCs 48 h p.i. with ZIKV. Scale bar, 50 μm.

(K) Representative immunostaining for ZIKV-E (green), CC3 (red), and DAPI (blue) of GSCs and forebrain-specific NPCs 72 h p.i. with ZIKV. Scale bars, 50 μm.

(L) Quantification of the percentage of $CC3^+$ cells in $DAPI^+$ cells for GSCs and NPCs 72 h p.i. with ZIKV.

(M) Cell viability of patient-derived cultures from GBM (387 and 3565), pontine glioma (3752 and 007), meningioma (CH-157MN, IOMM-LEE), ependymoma (EP1), and medulloblastoma cell lines (DAOY, D283, HDMB03, D341) 72 h after ZIKV infection. Experiments were performed in two biological replicates with three technical repeats. Values represent mean ± SEM. NS, no significance. ****$p < 0.0001$ by one-way ANOVA.

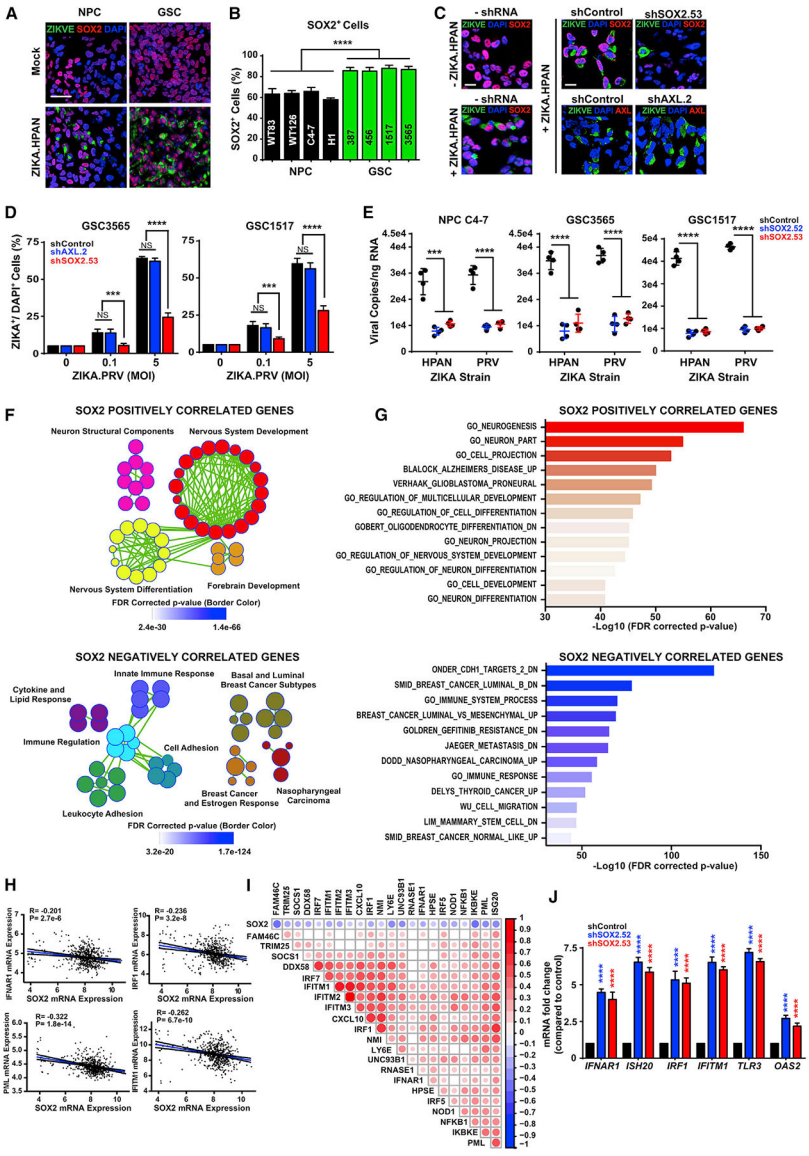

Figure 2. SOX2 Mediates Infection of GSCs Associated with Repression of Innate Antiviral Responses

(A) Representative immunostaining for ZIKV-E (green), SOX2 (red), and DAPI (blue) of GSCs and forebrain-specific hiPSC-derived NPCs 48 h p.i. with ZIKV. Scale bar, 50 μm.

(B) Quantification of the percentage of $SOX2^+$ cells in $DAPI^+$ cells for GSCs and NPCs 48 h p.i. with ZIKV.

(C) Representative immunostaining for ZIKV-E (green), SOX2 or AXL (red), and DAPI (blue) of GSCs (GSC3565) without transduction (shRNA) or transduced with control shRNA (shCONT), AXL shRNA (shAXL.2), or SOX2 shRNA (shSOX2.53) for 72 h and then 48 h with ZIKV infection. Scale bars, 100 μm.

(D) Quantification of the percentage of $ZIKV^+$ cells in $DAPI^+$ cells in GSCs 1517 and 3565 under conditions for (C), with a range of ZIKV infection.

(E) Viral copy number by qRT-PCR of GSCs (GSC3565 or GSC1517) or NPC C4–7 transduced with either shCONT or SOX2 shRNA (shSOX2.52 or shSOX2.53) for 72 h

and then either exposed to mock conditions or infected with ZIKV for another 72 h. All comparisons are versus shCONT.

(F) Gene set enrichment (GSE) bubble plots showing pathways positively (top, $r > 0.4$) or negatively (bottom, $r < -0.4$) correlated with *SOX2* expression in the TCGA GBM HG-U133A microarray dataset. Each circle represents an enriched pathway, with the border color indicating the false discovery rate (FDR)-corrected p value.

(G) GSE graph showing the top pathway enrichments positively or negatively correlated with *SOX2* as described in (F).

(H) Correlation of mRNA levels of SOX2 with IFNAR1, IRF1, promyelocytic leukemia (PML), and IFITIM1 from the TCGA GBM HG-U133A microarray dataset.

(I) Correlation between *SOX2* with ISGs from the TCGA GBM HG-U133A microarray dataset. The size and color of the dots indicate the degree of correlation ($p < 0.001$). Blank cells indicate a non-significant correlation.

(J) qPCR of ISGs (*IFNAR-1*, *ISH20*, *IRF1*, *IFITM1*, *TLR3*, and *OAS2*) in GSCs (GSC3565) transduced with either shCONT or SOX2 shRNA (shSOX2.52 or shSOX2.53).

Experiments were performed in two biological replicates with three technical repeats. Values represent mean ± SEM. **$p < 0.001$, ****$p < 0.0001$ by one-way ANOVA.

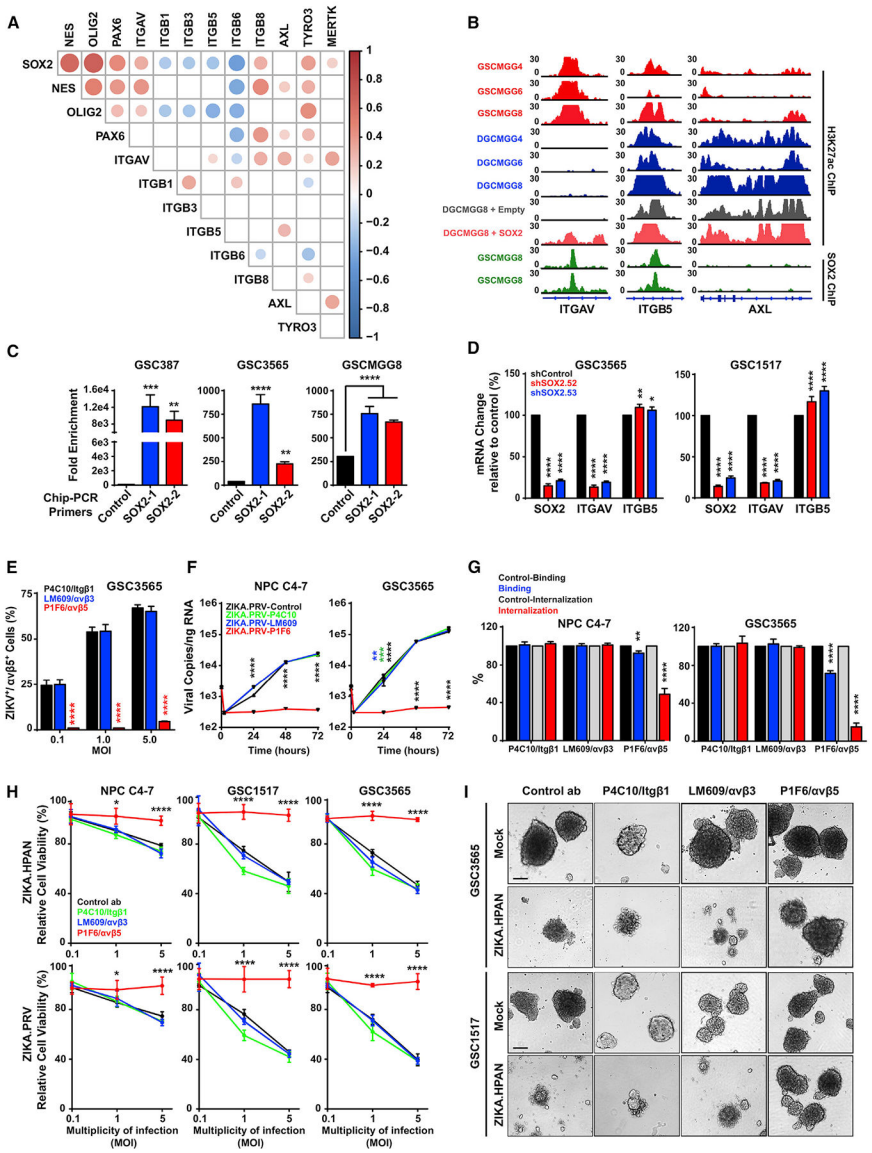

Figure 3. SOX2 Regulates Integrin α_V in GSCs, and Integrin $\alpha_V\beta_5$ Mediates ZIKV Infection in GSCs

(A) Correlation between *SOX2* mRNA expression with *ITGAV*, *Nestin* (*NES*), *PAX6*, *OLIG2*, *ITGB1*, *ITGB3*, *ITGB5*, *ITGB6*, *ITGB8*, *AXL*, *TYRO3*, and *MERTK* levels from the TCGA GBM HG-U133A microarray dataset. Size and color indicate the degree of correlation ($p < 0.001$), with blank cells indicating a non-significant correlation.

(B) ChIP-seq for H3K27ac or SOX2 at the *ITGAV*, *ITGB5*, and *AXL* loci in matched GSCs and DGCs and following SOX2 overexpression. Data were derived from GSE54792 and GSE17312.

(C) ChIP-PCR assessing SOX2 occupancy at the ITGAV locus with two distinct sequences (denoted SOX2–1 and SOX2–2) in three GSC lines (387, 3565, and MGG8).

(D) mRNA levels of *SOX2*, *ITGAV*, and *ITGB5* by qPCR for GSCs (GSC3565 or GSC1517) transduced with either shCONT or SOX2 shRNA (shSOX2.52 or shSOX2.53). p values indicate comparisons with shCONT.

(E) GSCs (GSC3565) were cultured with an IgG control antibody (LM142) or one of three neutralizing antibodies against integrins (Itgβ_1, 4C10; $\alpha_v\beta_3$, LM609; $\alpha_v\beta_5$, P1F6; 50 μg/mL) and then exposed to mock conditions or infection with ZIKV. The fraction of GBM integrin $\alpha_v\beta_5^+$ cells was assessed by immunofluorescence 72 h p.i. with ZIKV.

(F) GSCs (GSC3565) or NPCs (C4–7) were cultured as in (E). The number of intracellular ZIKV viral particles was quantified by qRT-PCR.

(G) Quantification of viral RNA by qRT-PCR in (F) was performed to assess surface binding or internalization with normalization to the IgG control.

(H) GSCs (GSC3565) were cultured as in (E). Cell viability was assessed 72 h p.i. with ZIKV.

(I) Representative bright-field images of GSCs (GSC3565 and GSC1517) that were cultured as in (E). Scale bars, 50 μm.

Experiments were performed in two biological replicates with three technical repeats. Values represent mean ± SEM. *$p < 0.05$, **$p < 0.01$, ****$p < 0.0001$ by one-way ANOVA.

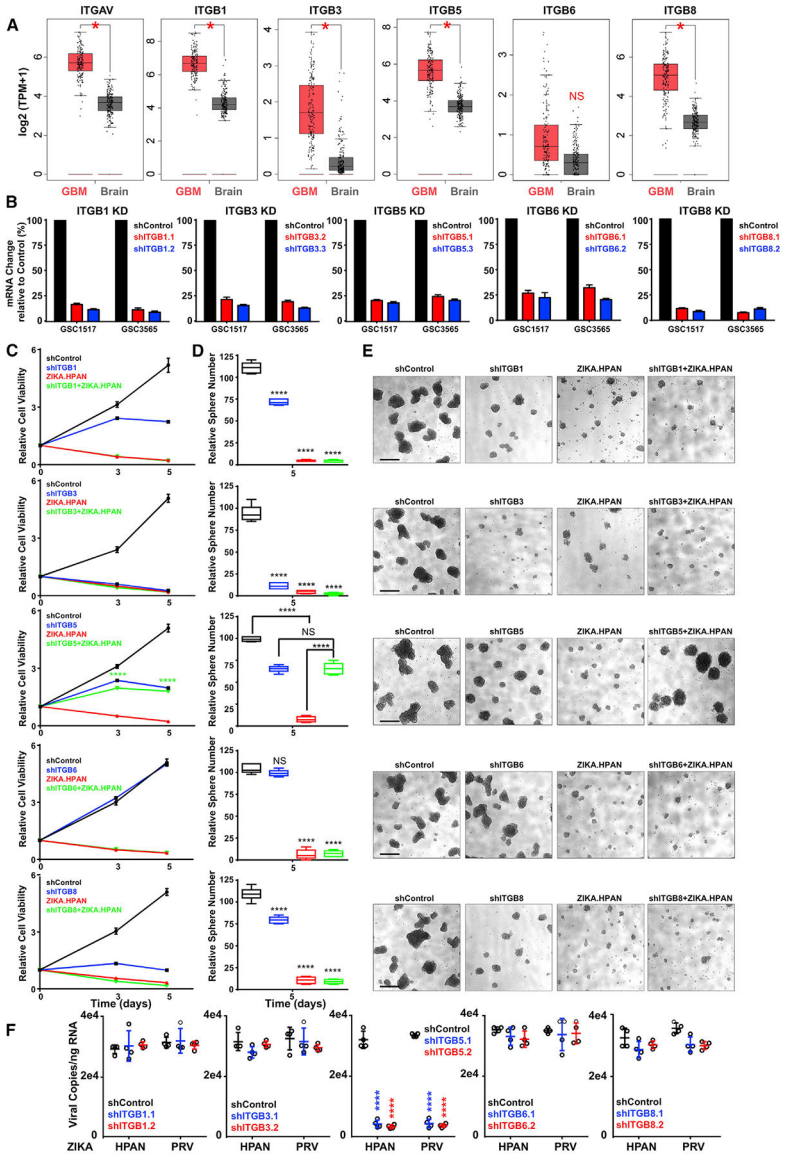

Figure 4. ZIKV Infection of GSCs Requires Integrin β_5

(A) Matched TCGA GBM and normal brain from the genotype-tissue expression (GTEx) dataset, showing the expression levels of selected integrins; log scale by Log2 (transcripts per million [TPM]+1). *p < 0.0001 (n = 163 samples for GBM, n = 207 samples for normal brain).

(B) mRNA expression of integrins following shRNA-mediated knockdown in two patient-derived GSCs (GSC1517 and GSC3565). Values were normalized to a non-targeting shCONT.

(C) Cell viability in GSC3565 on days 0, 3, and 5 following treatment with integrin-targeting shRNAs, ZIKV, or a combination.

(D) Quantification of the number of spheres formed by GSCs on day 5 following treatment with integrin-targeting shRNAs, ZIKV, or a combination.

(E) Representative images of spheres derived from GSC3565 (C and D). Scale bars, 100 μm.

(F) ZIKV infectivity assessed by qRT-PCR on patient-derived GSCs transduced with either shCONT or one of two non-overlapping shRNAs targeting integrin β subunits that paired with integrin α_V.

Two biological replicates with three technical repeats were performed. Data presented as mean ± SEM. ****$p < 0.0001$ by one-way ANOVA.

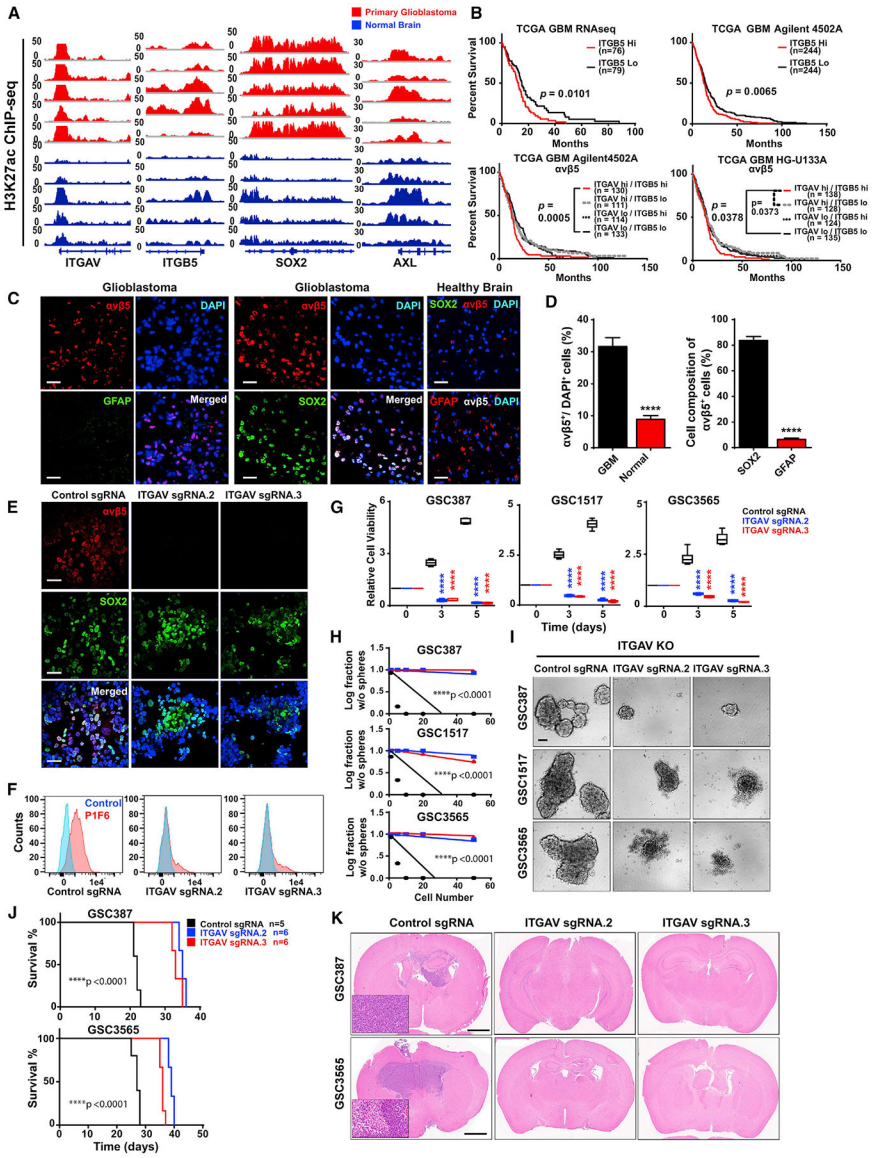

Figure 5. Integrin $\alpha_v\beta_5$ Maintains GSCs

(A) H3K27ac ChIP-seq of primary GBM (red, n = 5 samples) and normal human brain (blue, n = 5 specimens) at the *ITGAV, ITGB5, SOX2*, and *AXL* loci.

(B) Kaplan-Meier survival curve of patients from the TCGA database. Patients were categorized into a “high” or “low” expression group based on the median mRNA expression of ITGB5 and integrin $\alpha_v\beta_5$ in RNA sequencing (RNA-seq), the Agilent 4502 microarray, or the HG-U133A microarray. The p values were calculated by log rank test.

(C) Immunostaining for integrin $\alpha_v\beta_5$ (red), GFAP (green), SOX2 (green), and DAPI (blue) of primary human GBM surgical biopsy specimens (n = 3) or normal human brain (n = 2). Scale bars, 100 μm.

(D) (Left) The fraction of $DAPI^+$ cells from Figure 4C that stained for integrin $\alpha_v\beta_5$. Right: the fraction of $SOX2^+$ and $GFAP^+$ cells in integrin $\alpha_v\beta_5^+$ GSCs. Values represent mean ± SEM. ****$p < 0.0001$ by two-tailed Student’s t test.

(E) Representative immunostaining of GSCs (GSC3565) for integrin $\alpha_v\beta_5$ (red), SOX2 (green), and DAPI (blue) after transduction with either a sgCONT or one of two sgRNAs targeting ITGAV. Scale bars, 100 μm.

(F) Flow cytometry analysis for three patient-derived GSCs (GSC387, GSC1517, and GSC3565) transduced with either sgCONTor one of two sgRNAs targeting ITGAV following incubation with an IgG control antibody (LM142) or an integrin $\alpha_v\beta_5$ antibody (P1F6).

(G) Cell viability of three patient-derived GSCs (GSC387, GSC1517, and GSC3565) transduced with either sgCONT or one of two sgRNAs targeting ITGAVs normalized to day 0. Values represent mean ± SEM. ****$p < 0.0001$ by one-way ANOVA.

(H) Neurosphere formation of three patient-derived GSCs (GSC387, GSC1517, and GSC3565) transduced with either sgCONT or one of two sgRNAs targeting ITGAV. Values represent mean ± SEM. ****$p < 0.0001$ by extreme limiting dilution analysis (ELDA).

(I) Representative bright-field images of (H) at 5 days. Scale bar, 50 μm.

(J) Kaplan-Meier survival curves for mice bearing GSCs (GSC387 and GSC3565) transduced with either sgCONT or one of two sgRNAs targeting ITGAV (sgCONT, n = 5; ITGAV sgRNA, n = 6). ****$p < 0.0001$ by log rank analysis.

(K) Representative H&E images from (J). Boxes show magnified sections. Scale bars, 50 μm.

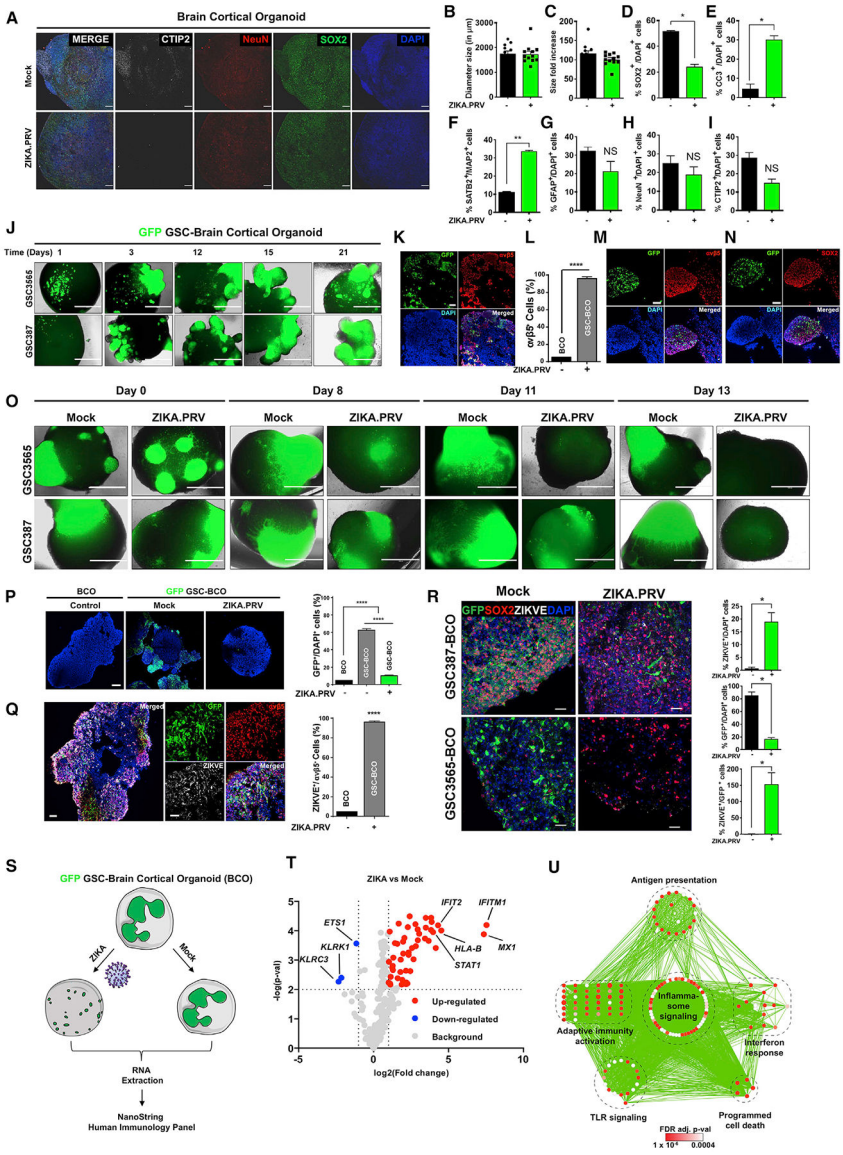

Figure 6. ZIKV Infection Preferentially Targets GBM in GBM-Brain Cortical Organoid (GSC-BCO) Models and Activates Viral Process and Type I IFN Signaling Pathways

(A) Representative images of mock- or ZIKV-infected BCOs stained with neuronal markers (CTIP2 and NeuN), a neural progenitor cell marker (SOX2), and DAPI. Scale bars, 100 μm.

(B) Quantification of BCO size p.i. with ZIKV. Significance was assessed by two-tailed Student's t test, and experiments were performed in two batches with 12 organoids per group per batch.

(C) BCO size fold change of ZIKV- and mock-treated groups over a period of 1 month.

(D) Quantification of $SOX2^+$ cells in ZIKV- versus mock-infected groups. *$p < 0.05$ by two-tailed Student's t test.

(E) Quantification of $CC3^+$ cells in ZIKV- versus mock-infected groups. *$p < 0.05$ by two-tailed Student's t test.

(F) Quantification of $SATB2^+$ cells within $MAP2^+$ cells in ZIKV- versus mock-infected groups. **$p < 0.01$ by two-tailed Student's t test.

(G) Quantification of $GFAP^+$ cells in ZIKV- versus mock-infected groups. N.S., not significant by two-tailed Student's t test.
(H) Quantification of $NeuN^+$ cells in ZIKV- versus mock-infected groups. N.S., not significant by two-tailed Student's t test.
(I) Quantification of $CTIP2^+$ cells in ZIKV- versus mock-infected groups. N.S., not significant by two-tailed Student's t test.
(J) Bright-field images of engraftment of two patient-derived GSCs (387 and 3565) transduced with GFP into human BCOs over a time course. Scale bars, 1 mm.
(K) Engrafted GSCs (GFP^+) with normal BCO immunostained for integrin $\alpha_v\beta_5$ (red), GFP (green), and DAPI (blue). Scale bars, 200 μm.
(L) Quantification of integrin $\alpha_v\beta_5{}^+$ cells in normal BCOs or GSC-BCOs. Values represent mean ± SEM. n = 6. ****p < 0.0001 by two-tailed Student's t test.
(M) Representative images of GFP-labeled GSC-BCOs immunostained for integrin $\alpha_v\beta_5$ (red), GFP (green), and DAPI (blue). Scale bars, 100 μm.
(N) Representative images of GFP-labeled GSC-BCOs immunostained for SOX2 (red), GFP (green), and DAPI (blue). Scale bars, 100 μm.
(O) Images of GFP-labeled GSC-GFP BCOs 13 days p.i. with ZIKV. Scale bars, 1 mm.
(P) Representative images of residual GSCs (green) and DAPI staining (blue) of GFP-labeled GSC-GFP BCOs cultured under mock conditions or with ZIKV for 2–4 weeks. Scale bars, 200 μm. The percentage of GFP^+ cells among $DAPI^+$ cells was quantified. Values represent mean ± SEM. n = 6. ****p < 0.0001 by two-way ANOVA.
(Q) Representative immunostaining for integrin $\alpha_v\beta_5$ (red), GFP (green), ZIKV-E (white), and DAPI (blue) of GFP-labeled GSC-GFP BCOs mock- or ZIKV-infected for 2–4 weeks. Scale bars, 200 μm (left) and 100 μm (center). The percentage of ZIKV-E^+ cells among integrin $\alpha_v\beta_5$ cells was quantified. Values represent mean ± SEM. n = 6. ****p < 0.0001 by two-tailed Student's t test.
(R) Representative images of 387 and 3565 GSC-BCOs with or without ZIKV, respectively, stained with SOX2, ZIKV-E, and DAPI. GFP shows the presence of GSCs (scale bars, 50 μm). ZIKV-E^+, GFP^+, and ZIKV-E^+ cells among GFP^+ cells were quantified by counting (two GSCs cell lines, two repeats, n = 12 organoids/group); *p < 0.05 by two-tailed Student's t test.
(S) Schematic of the experiment design.
(T) Volcano plot showing differences between GSC-BCO ZIKV versus GSC-BCO mock. 113 genes were differentially expressed (greater than 1.5-fold) between these two groups (*p < 0.05).
(U) Network analysis of genes differentially expressed upon ZIKV infection, represented as a bubble plot.

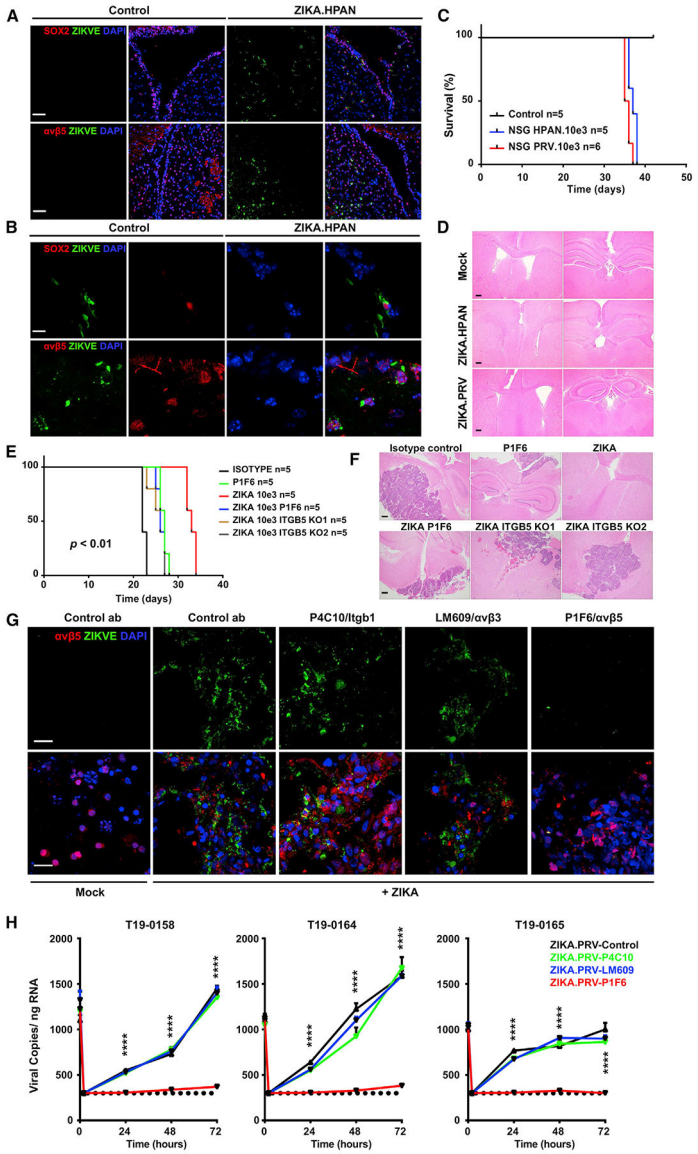

Figure 7. Integrin $\alpha_v\beta_5$ Mediates *In Vivo* ZIKV Targeting of GSCs in Mouse Models and in Human GBM

(A) Immunostaining of the subventricular zone (SVZ) of mice 72 h following ZIKV infection ZIKV-E (green), SOX2 (red, top panels), and integrin $\alpha_v\beta_5$ (red, bottom panels). Scale bars, 50 μm.

(B) Higher magnification of images from (A), demonstrating ZIKV infection of $SOX2^+$ (top panels) and integrin $\alpha_v\beta_5^+$ cells. Scale bars, 10 μm.

(C) Survival of ZIKV-infected NSG mice from (A) was plotted by the Kaplan-Meier method.

(D) ZIKV-infected brains from the mice in (A) were collected upon death, and histology was assessed by H&E staining. Scale bars, 20 μm.

(E) Survival of NSG mice following implantation of GSCs treated with isotype control, P1F6 antibody, ZIKV, combined P1F6 and ZIKV, combined CRISPR knockout (KO) of integrin β_5 (sgRNA1 sgRNA2) with ZIKV inoculation, analyzed by log rank test; $p < 0.01$.

(F) H&E staining of tumor-bearing brains from (E). Scale bars, 50 μm.
(G) Intraoperative brain slices from GBM patients were pre-incubated with an IgG control antibody or an integrin-blocking antibody under mock conditions or upon ZIKV infection (10e3 FFU). Slices then underwent immunofluorescence staining for ZIKV-E (green), integrin $\alpha_v\beta_5$ (red), and DAPI (blue). Scale bars, 10 μm.
(H) Intraoperative brain slices from GBM patients were pre-incubated with an IgG control antibody or an integrin-blocking antibody under mock conditions or upon ZIKV infection. Slices then underwent a viral RNA copy assay by qRT-PCR. Experiments were performed in two biological replicates with three technical repeats. Values represent mean ± SEM. ****$p < 0.0001$ by one-way ANOVA.

KEY RESOURCES TABLE

REAGENT or RESOURCE	SOURCE	IDENTIFIER
Antibodies		
Rabbit polyclonal antibody to SOX2	Abcam	Cat# ab97959; RRID:AB_2341193
Mouse monoclonal antibody to ZIKVE	EMD Millipore	Cat# MAB10216; RRID:AB_827205
Rabbit Cleaved Caspase3 antibody	Cell signaling	Cat# 9664; RRID:AB_2070042
Rabbit polyclonal antibody to AXL	Abcam	Cat# ab32828; RRID:AB_725598
Rabbit polyclonal antibody to GFAP (Poly284000)	Biolegend	Cat# 840001; RRID:AB_2565444
Mouse monoclonal antibody to beta-actin	Sigma-Aldrich	Cat# A5316; RRID:AB_476743
Rabbit monoclonal antibody to $\alpha_v\beta_5$	Absolute Antibody	Cat# Ab00888
Mouse monoclonal antibody to TUBB3	Thermofisher	Cat# MA1-118; RRID:AB_2536829
PE Mouse IgG1, κ Isotype Ctrl (FC) Control Antibody [Clone: MOPC-21]	Biolegend	Cat# 400113; RRID:AB_326435
Alexa Fluor 488 conjugated anti-mouse	Thermofisher	Cat# A-11001; RRID:AB_2534069
Alexa Fluor 594 conjugated anti-rabbit	Thermofisher	Cat# A-11012; RRID:AB_2534079
Alexa Fluor 594 conjugated anti-rat	Thermofisher	Cat# A-11007; RRID:AB_10561522
Alexa Fluor 647 conjugated anti-goat	Thermofisher	Cat# A-21447; RRID:AB_2535864
Anti-rabbit IgG, HRP-linked Secondary Antibody	Cell Signaling	Cat# 7074; RRID:AB_2099233
Anti-mouse IgG, HRP-linked Secondary Antibody	Cell Signaling	Cat# 7076; RRID:AB_330924
donkey anti-goat IgG-HRP-lined Secondary Antibody	Santa Cruz Biotechnology	Cat# sc-2020; RRID:AB_631728
Donkey anti-Rabbit IgG (H+L) Highly Cross-Adsorbed Secondary Antibody, Alexa Fluor 488	Life Technologies	Cat# A-21206; RRID:AB_2535792
Normal Goat IgG antibody (negative control for ChIP-PCR)	R & D Systems	Cat# AB-108-C; RRID:AB_354267
Rabbit monoclonal (14C10) antibody to GAPDH	Cell Signaling	Cat# 2118; RRID:AB_561053
Rabbit polyclonal antibody to CTIP2	US Biological	Cat# B0807-13E2; RRID:AB_2064140
Mouse monoclonal antibody to NeuN	PhosphoSolutions	Cat# 538-FOX3; RRID:AB_2560943
Rat monoclonal antibody to ITGA6	Thermofisher	Cat# 17-0495-82; RRID:AB_2016694
Chicken polyclonal antibody to MAP2	Abcam	Cat# ab5392; RRID:AB_2138153
Rabbit monoclonal antibody to SATB2	RevMAb Biosciences	Cat# 31-1251-00; RRID:AB_2783604
LM609 antibody	EMD Millipore	Cat# MAB1976; RRID:AB_2296419
P1F6 antibody	EMD Millipore	Cat# MAB1961Z; RRID:AB_94466
Bacterial and Virus Strains		
One Shot™ Stbl3™ Chemically Competent E. coli	Thermofisher	Cat# C737303
ZIKA.HPAN	BEI Resources	NR-50210
ZIKA.PRV	BEI Resources	NR-50240
Chemicals, Peptides, and Recombinant Proteins		
Neurobasal-A Medium	Life Technologies	Cat# A2477501
GlutaMAX Supplement	Life Technologies	Cat# 35050061
MEM nonessential amino acids	Thermofisher	Cat# 11140-050
Sodium Pyruvate	Life Technologies	Cat# 11360070
N2 NeuroPlex	Gemini Bio-Products	Cat# 400163
Gem21 NeuroPlex	Gemini Bio-Products	Cat# 400160

REAGENT or RESOURCE	SOURCE	IDENTIFIER
B27-supplement w/o Vitamin A	Life Technologies	Cat# 12587010
Recombinant Human EGF Protein	R&D Systems	Cat# 236-EG-01M
Recombinant Human FGF basic, 145 aa (TC Grade) Protein	R&D Systems	Cat# 4114-TC-01M
Recombinant Human BDNF	Peprotech	Cat# 450-02
Recombinant Human GDNF	Peprotech	Cat# 450-10
Recombinant Human NT-3	Peprotech	Cat# 450-03
L-Ascorbic acid	Sigma-Aldrich	Cat# A4403
N6,20-O-Dibutyryladenosine 30,50-cyclic monophosphate sodium salt	Sigma-Aldrich	Cat# D0627
Stemolecule SB431542	StemGent	Cat# 04-0010-10
Dorsomorphin	R&D Systems	Cat# 3093
ROCK inhibitor (Ri) Y-27632 dihydrochloride	Tocris	Cat# 125410
StemPro Accutase Cell Dissociation Reagent	Thermofisher	Cat# A1110501
Penicillin-Streptomycin (10,000 U/mL)	Thermofisher	Cat# 15140122
TrypLE™ Express Enzyme (1X), no phenol red	Thermofisher	Cat# 12604021
Fetal Bovine Serum, qualified, US origin	Thermofisher	Cat# 26140079
NuPage 4%−12% Bis-Tris gels	Invitrogen	NP0321BOX
PVDF membranes	EMD Millipore	Cat# ISEQ00010
Matrigel hESC-Qualified Matrix	Corning	Cat# 354277
LipoD293™ In Vitro DNA Transfection Reagent	SignaGen Laboratories	Cat# SL100668
JetPrime transfection reagent	Polyplus	Cat# 89129-926
qScript cDNA synthesis kit	Quanta	Cat# 101414-106
EndoFree Plasmid mini kit	Omega	Cat# D6948
Click-iT EdU imaging Kit with Alexa 594	Molecular probes	Cat# C10086
TUNEL Assay Kit - HRP-DAB	Abcam	Cat# ab206386
PowerUp™ SYBR™ Green Master Mix	Thermofisher	Cat# A25742
Radiant™ Green Hi-ROX qPCR Kit, 5000 × 20µl Reactions,50 × 1µL	Alkali scientific inc	Cat# QS2050
Qiagen RNeasy Mini Plus kit	Qiagen	Cat# 74134
QIAamp Viral RNA Mini Kit	Qiagen	Cat# 52904
Cell Titer-Glo™ Cell Viability Reagent	Promega	Cat# G7570
Dead Cell Apoptosis Kit with Annexin V Alexa Fluor™ 488	Thermofisher	Cat# V13241
High Capacity cDNA Reverse Transcription Kit	Life Technologies	Cat# 4368814
Lenti-X Concentrator	Clontech (Takara Bio USA)	Cat# 631232
Pronase	Roche Applied Science	Cat# 10165921001
Bradford assay	Bio-Rad Laboratories	Cat# 5000006
Mission Lentiviral Packaging Mix	Sigma-Aldrich	Cat# SHP001
Quick-RNA MiniPrep Plus kit	Zymo Research	Cat# R1055
TRIzol reagent	Sigma-Aldrich	Cat# T9424
TaqMan® Universal Master Mix II, no UNG	Thermofisher	Cat# 4440043
Critical Commercial Assays		
VECTASHIELD with DAPI	Vector Laboratories	Cat# H-1200; RRID:AB_2336790

REAGENT or RESOURCE	SOURCE	IDENTIFIER
Experimental Models: Cell Lines		
293FT Cell Line	Thermofisher	Cat# R70007
ENSA (ENS-tem-A)	EMD Millipore	Cat# SCC003, RRID:CVCL_GS51
NSC11	Alstem	Mack et al., 2019
NM53	Cleveland Clinic	N/A
NM55	Cleveland Clinic	N/A
NM177	Cleveland Clinic	N/A
NPC C4–7	Gage lab, Salk	Schafer et al., 2019
hNP1 (STEMEZ hNP1)	Neuromics	Cat# HN60001
H1 ESC	RCB	Cat# RCB1778, RRID:CVCL_N541
NPC194	Cleveland clinic	Mack et al., 2019
EP1	DKFZ	Milde et al., 2011
fh NPC	Clontech Stem Cell Line Kits	Y40050
WT83 iPS and NPC	Muotri Lab, UCSD	N/A
WT126 iPS and NPC	Muotri Lab, UCSD	RRID:CVCL_HA44
DAOY	ATCC	Cat# HTB-186, RRID:CVCL_1167
D283	ATCC	Cat# HTB-185, RRID:CVCL_1155
HDMB03	DSMZ	Cat# ACC-740, RRID:CVCL_S506
D341	ATCC	Cat# HTB-187, RRID:CVCL_0018
HNA/Human Astrocyte kit	Thermofisher	Cat# N7805200
Experimental Models: Organisms/Strains		
NSG (NOD.Cg-*Prkdc*^{scid}*Il2rg*^{tm1Wjl}/SzJl)	The Jackson Laboratory	JAX:005557
Recombinant DNA		
pCMV-dR8.2 dvpr	Addgene	Plasmid# 8455, RRID:Addgene_8455
pCI-VSVG	Addgene	Plasmid# 1733, RRID:Addgene_1733
LentiCRISPR v2	Addgene	Plasmid# 52961, RRID:Addgene_52961
SOX2 shRNA: shSOX52	Sigma-Aldrich	TRCN0000355694
SOX2 shRNA: shSOX53	Sigma-Aldrich	TRCN0000355638
Non-targeting Control shRNA: shCONT	Sigma-Aldrich	pLKO.1 Non-targeting Vector (SHC002)
psPAX2	Addgene	Plasmid# 12260, RRID:Addgene_12260
pMD2.G	Addgene	Plasmid# 12259, RRID:Addgene_12259
pSIN-hPGK-EGFP-WPRE	Peter Wang's lab, UCSD	N/A
Software and Algorithms		
GlioVis	Bowman et al., 2017	http://gliovis.bioinfo.cnio.es
DeepTools (v2.4.1)	Ramírez et al., 2016	http://deeptools.readthedocs.io/en/latest/index.html
Extreme limiting-dilution analysis	Hu and Smyth, 2009	http://bioinf.wehi.edu.au/software/elda/
Trim Galore v0.4.3		https://www.bioinformatics.babraham.ac.uk/projects/trim_galore

REAGENT or RESOURCE	SOURCE	IDENTIFIER
FASTQC		https://www.bioinformatics.babraham.ac.uk/projects/fastqc/
Gene Set Enrichment Analyses	Mootha et al., 2003; Subramanian et al., 2005	http://software.broadinstitute.org/gsea/index.jsp
Synthego ICE Analysis		https://ice.synthego.com/#/
Gene Expression Profiling Interactive Analyses (GEPIA)	Tang et al., 2017	http://gepia.cancer-pku.cn/about.html
Synergy Finder	Ianevski et al., 2017	N/A
HOMER	Heinz et al., 2010	http://homer.ucsd.edu/homer/
DESeq2	Love et al., 2014	https://bioconductor.org/packages/release/bioc/html/DESeq2.html
BedTools	Quinlan and Hall, 2010	http://bedtools.readthedocs.io/en/latest/
Cytoscape	Shannon et al., 2003	http://www.cytoscape.org/
TXImport	Soneson et al., 2016	https://bioconductor.org/packages/release/bioc/html/tximport.html
GraphPad Prism	Commercially available	https://www.graphpad.com/scientific-software/prism/
Adobe Illustrator	Commercially available	https://www.adobe.com/
R Programming Language		https://www.r-project.org/
R Studio	Commercially available	https://www.rstudio.com/
Microsoft Office	Commercially available	https://www.office.com/
IGV (Integrative Genomics Viewer)	Robinson et al., 2011; Thorvaldsdottir et al., 2013	https://software.broadinstitute.org/software/igv/
Image Lab	Commercially available	http://www.bio-rad.com/en-us/product/image-lab-software?ID=KRE6P5E8Z
Gene Pattern	Reich et al., 2006	https://software.broadinstitute.org/cancer/software/genepattern/
ImageJ / FIJI	Schindelin et al., 2012	https://fiji.sc/
Other		
BD LSR Fortessa Flow Cytometer	Beckman	N/A
ZEISS 580 Confocal Microscope	ZEISS	N/A
Zeiss Apotome microscope	ZEISS	N/A
NanoString nCounter system	NanoString	N/A
Applied Biosystems 7500HT cycler	Applied Biosystems	N/A
nSolver software	NanoString	N/A
CFX96 Touch Detection System	Bio-Rad	N/A
Glioblastoma Stem Cell and Differentiated Glioblastoma Cell H3K27ac ChIP-seq and RNA-seq data	Suvà et al., 2014	GEO: GSE54792
Glioblastoma Tissue H3K27ac ChIP-seq data	Liu et al., 2015	GEO: GSE72468
Glioblastoma Tissue H3K27ac ChIP-seq data	Wang et al., 2017b	GEO: GSE101148
Glioblastoma single-cell RNA-seq data	Darmanis et al., 2017	GEO: GSE84465
Normal Brain single-cell RNA-seq data	Pollen et al., 2015	Supplemental Data
Normal Brain Tissue H3K27ac ChIP-seq Data	Encode Project	https://www.encodeproject.org/files/ENCFF398LQI/@@download/ENCFF398LQI.bam
Normal Brain Tissue H3K27ac ChIP-seq Data	Encode Project	https://www.encodeproject.org/files/ENCFF317ZJQ/@@download/ENCFF317ZJQ.bam

REAGENT or RESOURCE	SOURCE	IDENTIFIER
Normal Brain Tissue H3K27ac ChIP-seq Data	Encode Project	https://www.encodeproject.org/files/ENCFF883QEJ/@@download/ENCFF883QEJ.bam
Normal Brain Tissue H3K27ac ChIP-seq Data	Encode Project	https://www.encodeproject.org/files/ENCFF858WMB/@@download/ENCFF858WMB.bam
Normal Brain Tissue H3K27ac ChIP-seq Data	Encode Project	https://www.encodeproject.org/files/ENCFF465XYF/@@download/ENCFF465XYF.bam
Normal Brain Tissue H3K27ac ChIP-seq Data	Encode Project	https://www.encodeproject.org/files/ENCFF042WIR/@@download/ENCFF042WIR.bam
Normal Brain Tissue H3K27ac ChIP-seq Data	Encode Project	https://www.encodeproject.org/files/ENCFF854IBQ/@@download/ENCFF854IBQ.bam
Normal Brain Tissue H3K27ac ChIP-seq Data	Encode Project	https://www.encodeproject.org/files/ENCFF258IAC/@@download/ENCFF258IAC.bam
Normal Brain Tissue H3K27ac ChIP-seq Data	Encode Project	https://www.encodeproject.org/files/ENCFF021NCO/@@download/ENCFF021NCO.bam
Normal Brain Tissue H3K27ac ChIP-seq Data	Encode Project	https://www.encodeproject.org/files/ENCFF866QWG/@@download/ENCFF866QWG.bam
Normal Brain Tissue H3K27ac ChIP-seq Data	Encode Project	https://www.encodeproject.org/files/ENCFF284YVJ/@@download/ENCFF284YVJ.bam
Normal Brain Tissue H3K27ac ChIP-seq Data	Encode Project	https://www.encodeproject.org/files/ENCFF300PEE/@@download/ENCFF300PEE.bam
Normal Brain Tissue H3K27ac ChIP-seq Data	Encode Project	https://www.encodeproject.org/files/ENCFF240QQV/@@download/ENCFF240QQV.bam
Normal Brain Tissue H3K27ac ChIP-seq Data	Encode Project	https://www.encodeproject.org/files/ENCFF592XMP/@@download/ENCFF592XMP.bam
Normal Brain Tissue H3K27ac ChIP-seq Data	Encode Project	https://www.encodeproject.org/files/ENCFF519BFV/@@download/ENCFF519BFV.bam
GlioVis	Bowman et al., 2017	http://gliovis.bioinfo.cnio.es